

1 Long-Term Atmospheric Emissions for the Coal Oil Point 2 Natural Marine Hydrocarbon Seep Field, Offshore California

3 Ira Leifer¹, Christopher Melton¹, Donald R. Blake²

4 ¹Bubbleology Research International, Solvang, CA 93463, United States

5 ²University of California, Irvine, Department of Chemistry, Irvine, CA 92697, United States

6 Correspondence to: Ira Leifer (Ira.Leifer@bubbleology.com)

7 **Abstract.** In this study, we present a novel approach for assessing nearshore seepage atmospheric emissions through
8 modeling of air quality station data, specifically, a Gaussian plume inversion model. Three decades of air quality
9 station meteorology and total hydrocarbon concentration, *THC*, data were analysed to study emissions from the Coal
10 Oil Point marine seep field offshore California. *THC* in the seep field directions was significantly elevated and
11 Gaussian with respect to wind direction, θ . An inversion model of the seep field anomaly, $THC(\theta)$, derived
12 atmospheric emissions. The model inversion is for the far field, which was satisfied by gridding the sonar seepage and
13 treating each grid cell as a separate Gaussian plume. This assumption was validated by offshore *in situ* offshore data
14 that showed major seep area plumes were Gaussian. Plume air sample THC was 85% methane, CH₄, and 20% carbon
15 dioxide, CO₂, similar to seabed composition, demonstrating efficient vertical plume transport of dissolved seep gases.
16 Air samples also measured atmospheric alkane plume composition. The inversion model used observed winds and
17 derived the three-decade-average (1990-2021) field-wide atmospheric emissions of 83,500±12,000 m³ THC day⁻¹.
18 Based on a 50:50 air to seawater partitioning, this implies seabed emissions of 167,000 m³ THC dy⁻¹. Based on
19 atmospheric plume composition, C₁-C₆ alkane emissions were 19, 1.3, 2.5, 2.2, 1.1, and 0.15 Gg yr⁻¹, respectively. If
20 CH₄ emissions were dispersed over the ~6.3 km² of 25x25 m² bins with sonar values above noise, we find 5.7 μM m⁻²
21 s⁻¹. The approach can be extended to derive emissions from other dispersed sources such as landfills, industrial sites,
22 or terrestrial seepage if source locations are constrained spatially.

24 1 Introduction

25 1.1 Seepage and methane

26 On decadal timescales, the important greenhouse gas, methane, CH₄, affects atmospheric radiative balance far more
27 strongly than carbon dioxide, CO₂ (IPCC, 2007, Fig. 2.21), yet CH₄ has large uncertainties for many sources (IPCC,
28 2013). Since pre-industrial times, CH₄ emissions have risen by a factor of ~2.5, and after stabilizing in the 1990s and
29 early 2000s, resumed rapid growth since 2007 (Nisbet et al., 2019). The significantly shorter lifetime of CH₄ than CO₂
30 argues for CH₄ regulatory priority as emission reductions (and changes to the radiative balance) manifest more quickly
31 as atmospheric concentrations decrease (Shindell, Faluvegi, Bell, & Schmidt, 2005). Further impetus for a CH₄ focus
32 is a recent estimate that 40% CH₄ emissions reductions are feasible at no net cost for the oil and gas, O&G, industry

33 (IEA, 2020), a major anthropogenic CH₄ source (IPCC, 2014). This is particularly salient given a recent estimate that
34 half of recent CH₄ increases are from the O&G industry (Jackson et al., 2020).

35
36 For 2008-2017, global CH₄ top-down emissions estimates are 576 Tg yr⁻¹; 1 Tg=10¹² g, (550-594 Tg yr⁻¹) whereas
37 bottom-up approaches find 737 Tg yr⁻¹ (594-881 Tg yr⁻¹). Anthropogenic sources for 2008-2017 were estimated at
38 336-376 Tg CH₄ yr⁻¹ based on bottom-up estimates. Natural sources include wildfires, wetlands, hydrates, and
39 geological seepage among others. Bottom-up estimates for natural sources are higher than top-down estimates
40 including for geological sources (Saunio et al., 2020). Geological sources (including seepage) are estimated at 63-80
41 Tg CH₄ yr⁻¹ with marine seepage estimated to contribute 20-30 Tg CH₄ yr⁻¹ (Etiope, Ciotoli, Schwietzke, & Schoell,
42 2019) or 5-10 Tg CH₄ yr⁻¹ (Saunio et al., 2020). For comparison, marine non-geological CH₄ emissions are estimated
43 at 4-10 Tg yr⁻¹. The broad range of this emissions estimate is based in part on the uncertainty in the fraction of seabed
44 emissions that reaches the atmosphere and the uncertainty in overall seabed emissions. Further complexity in assessing
45 geological seepage CH₄ emissions arise because both seepage and O&G emissions source from the same geological
46 reservoirs (Leifer, 2019) and thus are isotopically similar (Schwietzke et al., 2016).

47
48 Seepage is where the migration of petroleum hydrocarbon gases and fluids in the lithosphere escape to the hydrosphere
49 and/or atmosphere from the reservoir formation which underlies a capping layer that seals the formation, allowing
50 hydrocarbon accumulation. Thus, seepage requires a migration pathway through the capping layer (Abrams, 2005),
51 or a capping layer that eroded away leaving an outcropping of the reservoir formation.

52
53 Marine seepage is widespread in every sea and ocean (Judd & Hovland, 2007). Quantitative seepage estimates (for
54 global budgets) are limited (though growing); see Leifer (2019) review and below for more recent. Fluxes for
55 individual marine seep vents and seep areas have been reported for the Gulf of Mexico (Johansen et al., 2020; Leifer
56 & MacDonald, 2003; Römer et al., 2019; T. C. Weber et al., 2014), the Black Sea (Greinert, McGinnis, Naudts, Linke,
57 & De Batist, 2010), the southern Baltic Sea (Heyer & Berger, 2000), various sectors of the North Sea (Borges,
58 Champenois, Gypens, Delille, & Harlay, 2016; Leifer, 2015; Römer et al., 2017), offshore Norway (Muyakshin &
59 Sauter, 2010; Sauter et al., 2006) offshore Svalbard in the Norwegian Arctic (Velo-Alarcón et al., 2019), offshore
60 Pakistan (Römer, Sahling, Pape, Bohrmann, & Spieß, 2012), the arctic Laptev Sea (Leifer, Chernykh, Shakhova, &
61 Semiletov, 2017), the East Siberian Arctic Sea (Shakhova et al., 2013), the South China Sea (Di, Feng, Tao, & Chen,
62 2020), New Zealand's Hikurangi Margin (Higgs et al., 2019), the Cascadia Margin (Riedel et al., 2018), and the Coal
63 Oil Point (COP) marine hydrocarbon seep field, hereafter COP seep field, in the northern Santa Barbara Channel,
64 offshore Southern California (Hornafius, Quigley, & Luyendyk, 1999), and for numerous individual vents in the field
65 (Leifer, 2010).

66
67 Most seep emission estimates are snapshot from short-term field campaigns. Seep emissions vary on timescales from
68 tidal (Leifer & Boles, 2005; Römer, Riedel, Scherwath, Heesemann, & Spence, 2016) to seasonal (Bradley, Leifer, &
69 Roberts, 2010) to decadal (Fischer, 1978; Leifer, 2019). Additional temporal variability arises from transient emissions

70 – pulses lasting seconds to minutes (Greinert, 2008; Schmale et al., 2015) to decades (Leifer, 2019). This shortcoming
71 is being addressed by benthic (seabed) observatories and cabled observatories, e.g., Wiggins, Leifer, Linke, and
72 Hildebrand (2015); Greinert (2008), Kasaya et al. (2009); Römer et al. (2016); Scherwath et al. (2019). Still, benthic
73 observatories are costly and thus uncommon.

74
75 Seepage contributes to oceanographic budgets and to a lesser extent, atmospheric budgets due to water column losses
76 with significant uncertainty in the partitioning. As a result, uncertainty in the atmospheric contribution is much larger
77 than the (significant) uncertainty in seabed emissions. Seepage partitioning between the atmosphere and ocean - where
78 microbial degradation occurs on timescales inversely related to concentration (Reeburgh et al., 1991), which depends
79 primarily on depth (Leifer & Patro, 2002) with little to none of deepsea seabed emissions reaching the atmosphere,
80 e.g., Römer et al. (2019). In contrast, very shallow seepage (meter scale) largely entirely reaches the atmosphere both
81 by direct bubble-mediated transfer and diffusive transport. For intermediate depths, the ocean/atmospheric
82 partitioning is complex and depends on depth, bubble flux, bubble size distribution, bubble interfacial conditions, and
83 other characteristics (Leifer & Patro, 2002). Whereas the indirect diffusive flux (proximate and distal) depends on
84 bubble dissolution depth (Leifer & Patro, 2002), turbulence vertical transport in the winter wave-mixed layer (Rehder,
85 Keir, Suess, & Rhein, 1999), microbial oxidation losses, and exchange through the sea-air interface.

86
87 A range of approaches have been used to estimate the sea-air flux. The most common is by measuring the atmospheric
88 and water concentrations and applying air-sea gas exchange theory for the measured wind speeds, e.g., Schmale,
89 Greinert, and Rehder (2005) for Black Sea seepage under weak wind speeds.

90
91 Sea-air exchange is a diffusive turbulence transfer process that depends on the air-sea concentration difference and
92 the piston velocity, k_T , which depends on gas physical properties, wind speed, u (Liss & Duce, 2005), wave
93 development (Zhao, Toba, Suzuki, & Komori, 2003), wave breaking (Liss & Merlivat, 1986), and surfactant layers at
94 low wind speeds that suppress gas exchange (Frew et al., 2004). k_T increases rapidly and non-linearly with u and has
95 been parameterized as piecewise linear functions (Wanninkhof, Asher, Ho, Sweeney, & McGillis, 2009) or as a cubic
96 function (Nightingale et al., 2000). Air-sea gas exchange theory is for (relatively) homogeneous atmospheric and
97 oceanographic fields (concentrations, winds, and wave development), and thus is inappropriate for point-source
98 (bubble-plume) emissions and for the near-field downcurrent plume, which tend to be heterogeneous.

99
100 Another approach uses seabed bubble size measurements or an assumed bubble size distribution to initialize a
101 numerical bubble propagation model to predict direct bubble-mediated atmospheric fluxes (Leifer et al., 2017; Römer
102 et al., 2017; Schneider von Deimling et al., 2011). The dissolved portion that evades to the atmosphere could be
103 addressed by a dispersive model coupled to an air-sea gas exchange model, though studies have not yet addressed this
104 component.

105

106 An alternate approach is to derive atmospheric emissions by plume inversion. Leifer, Luyendyk, Boles, and Clark
107 (2006) derived emissions for a blowout from Shane Seep in the COP seep field by a plume inversion. This neglected
108 the portion that dissolves during bubble rise and drifts downcurrent, out of the bubble plume's vicinity before sea-air
109 gas transfer into the atmosphere. Note dissolved gas evasion in the plume vicinity contributes to the inversion
110 emissions estimate.

111

112 **1.2 Study motivation**

113 In this study, we present a novel approach for assessing nearshore seepage atmospheric emissions – air quality station
114 data modeling, specifically using a Gaussian plume inversion model. This model requires that source locations are
115 mapped, spatially stable, and lie within a fairly constrained distance range band. These conditions are met for the COP
116 seep field, which is near the West Campus air quality Station (WCS). COP seep field lies in shallow coastal waters of
117 northern Santa Barbara Channel, CA. Spatial constraint is provided by geological structures, such as faults, that
118 constrain emission locations. The Gaussian plume model assumes the source is in the far field, whereas WCS is in the
119 nearfield for the extensive COP seep field. To satisfy the far field criterion, the source was gridded and each grid cell's
120 emissions treated as a distinct (distant) Gaussian plume. This characterization was validated in an offshore survey of
121 several focused COP seep field seepage areas, which were well-modeled as Gaussian plumes.

122

123 Thus, this study demonstrates an approach to deriving emissions from air quality station data for an area source such
124 as natural marine seepage. This approach could be used to derive emissions from other dispersed sources such as
125 landfills, industrial sites, or natural terrestrial seepage where the source locations can be constrained spatially.

126

127 **1.3 Water column marine seabed seepage fate**

128 Seep seabed CH₄ partitioning between the atmosphere and water column depends on seabed depth and emission
129 character – as bubbles, bubble plumes (Leifer & Patro, 2002), or dissolved CH₄. Dissolved CH₄ migration through the
130 sediment is oxidized largely by near seabed microbes (Reeburgh, 2007), termed the microbial filter, negating its
131 contribution, leaving only bubble-mediated flow.

132

133 As seep bubbles rise, they dissolve, losing gas to the surrounding water at a rate that decreases with time; smaller and
134 more soluble gases dissolve faster than larger and less soluble gases, i.e., fractionation (Leifer & Patro, 2002).
135 Additionally, larger bubbles transport their contents upwards more efficiently than smaller bubbles (Leifer et al.,
136 2006). Sufficiently large bubbles reach the sea surface with a significant fraction of their seabed CH₄ from depths of
137 even hundreds of meters (Solomon, Kastner, MacDonald, & Leifer, 2009). There are synergies, too with higher plume
138 fluxes driving a stronger upwelling flow that transports plume fluids with dissolved gases upwards towards the surface
139 where air-sea gas exchange drives evasion (Leifer, Jeuthe, Gjøsend, & Johansen, 2009). Another synergy arises from

140 elevated dissolved plume CH₄ concentration (Leifer, 2010; Leifer et al., 2006), which slows dissolution. Also, bubbles
141 are oil-coated, which slows dissolution.

142
143 Moreover, gases in bubbles that dissolve in the wave-mixed layer (or reach it by the upwelling flow) then diffuse to
144 the air-sea interface due to wave and wind turbulence. Note, microbial degradation removes a portion of the dissolved
145 CH₄, which therefore never reaches the air-sea interface. Thus, there are two timescales that govern the fraction that
146 evades – the microbial degradation timescale, which decreases as concentrations increase, and the diffusion timescale,
147 which decreases with increasing wind speed. As a result, there is a dissolved plume that drifts downcurrent, from
148 which evasion creates a linear-source atmospheric plume, with dissolved plume concentrations slowly decreasing with
149 time (downcurrent distance) from sea-air gas exchange losses, microbial oxidation, and dispersion.

150

151 **1.4 Atmospheric Gaussian plumes**

152 Strong focused atmospheric plumes are created from the seep plume bubble bursting at the sea surface and from
153 dissolved gas evasion within the bubble surfacing footprint. This evasion is enhanced by water-side turbulence from
154 rising and bursting bubbles (Leifer et al., 2015). Atmospheric plume evolution is described by the Gaussian plume
155 model (Hanna, Briggs, & Hosker Jr., 1982), which relates downwind concentrations to wind transport and turbulence
156 dispersion and is the basis of the inversion calculation (see **Supp. Sec. S1** for details).

157

158 **1.5 Setting**

159 **1.5.1 The Coal Oil Point seep field**

160 The COP seep field (**Fig. 1**) is one of the largest seep fields in the world, with estimated 1995-1996 seabed emissions,
161 E_B , of $1.5 \times 10^5 \pm 2 \times 10^4$ m³ THC dy⁻¹ (Hornafius et al., 1999). Hereafter emissions and concentrations are for total
162 hydrocarbon, THC, unless noted. Clark, Washburn, Hornafius, and Luyendyk (2000) estimated that half the COP seep
163 field E_B reach the atmosphere in the near field. This is due to shallowness, bubble oiliness, high plume bubble densities,
164 and turbulence mixing within the wave mixed layer.

165

166 Geological structures play a critical role in the spatial distribution of seepage (Leifer, Kamerling, Luyendyk, & Wilson,
167 2010), which lies along several trends in waters from a few meters to ~85 m deep. These trends follow geologic
168 structures including anticlines, synclines, and faults in the reservoir formation, the Monterey Formation. Faults provide
169 migration pathways with seepage scattered non-uniformly along the trends, including focused seep areas that are
170 highly active, localized, and often are associated with crossing faults and fractures (Leifer et al., 2010). Seepage in
171 these areas typically surrounds a focus and decreases with distance, primarily along linear trends (Leifer, Boles,
172 Luyendyk, & Clark, 2004). See **Supp. Table S3** for informal names and locations of selected focused seep areas.

173

174 **1.5.2 Coal Oil Point seep field emissions and composition**

175 COP seep field sources from the South Ellwood oil field whose primary source rock is Monterey Formation, which is
176 immature to marginally mature. Petroleum gases from marine organic materials have relatively higher proportion of
177 ethane, propane, butane, etc., relative to methane as compared to petroleum gases from terrestrial organic materials.
178 The wet gas fraction (C_2-C_5/C_1-C_5) indicates a thermogenic origin of greater than 0.05 (Abrams, 2017). Of the
179 saturated alkanes, the alkenes (olefins) are of biological origin. Additionally, the ethane/ethene ratio and
180 propane/propene ratios can be indicators of seep gas biogenic modification with values above 1000 indicating purely
181 thermogenic origin (Abrams, 2017; Bernard, Brooks, & Zumberge, 2001).

182
183 In this study, we analyse WCS (located at $34^\circ 24.897'N$, $119^\circ 52.770'W$) atmospheric THC. Clark, Washburn, and
184 Schwager (2010) report average seep field seabed CH_4 , CO_2 , and non-methane hydrocarbons (NMHC), of 76.7, 15.3,
185 and 7.7%, respectively, with Trilogy Seep seabed compositions of 67, 21, and 7.8%, respectively. With respect to
186 alkanes, seabed bubbles are 90.4% CH_4 and 8.6% NMHC. CO_2 rapidly escapes the bubbles and is negligible (<1%)
187 at the sea surface. At the sea surface, CH_4 in bubbles is ~90% with NMHC making up the remaining 10%, neglecting
188 air gases (Clark et al., 2010). Note, whereas seep THC is predominantly CH_4 , THC from terrestrial directions arises
189 from NMHC from traffic and other anthropogenic sources as well as CH_4 from pipeline leaks, terrestrial seeps, etc.

190
191 **1.5.3 Northern Santa Barbara Channel climate**

192 Diurnal and seasonal wind cycles are important to the atmospheric transport of COP seep field emissions. The Santa
193 Barbara climate is Mediterranean with a dry season and a wet seasons when storms occur infrequently (Dorman &
194 Winant, 2000). The semi-permanent eastern Pacific high-pressure system plays a dominant controlling role in weather
195 in the Santa Barbara coastal plain. This high-pressure system drives light winds and strong temperature inversions that
196 act as a lid that restricts convective mixing to lower altitudes. The coastal California boundary layer is shallow, 0 to
197 800 m (Edinger, 1959), generally 240-300 m around Santa Barbara (Dorman & Winant, 2000). Additionally, coastal
198 mountains provide physical barriers to transport (Lu, Turco, & Jacobson, 1997).

199
200 As a coastal environment, the land/sea breeze is important to overall wind-flow patterns with weak offshore night
201 winds and stronger onshore afternoon winds (Dorman & Winant, 2000). In coastal Santa Barbara, warming on
202 mountaintops and more interior arid lands relative to cooler marine temperatures drives the sea breeze. Downslope
203 nocturnal flows warm nocturnal surface temperatures, moderating the coastal diurnal temperature cycle (Hughes, Hall,
204 & Fovell, 2007).

205
206 Typical morning winds are calm and offshore and often accompanied by a cloud-filled marine boundary layer, 50–
207 150 m thick (Lu et al., 1997). The marine layer usually (but not always) “burns off” mid-morning after which
208 temperatures rise, the boundary layer thickens and winds shift clockwise from offshore to eventually prevailing

209 westerlies aligned with the coastal mountains. Midday through late afternoon and even evening, winds strengthen,
210 often leading to whitecapping before the boundary layer collapses and winds resume the nocturnal pattern.
211

212 **2 Methods**

213 **2.1 West Campus Station data**

214 WCS data includes wind speed, u , and direction, θ , by a vane anemometer (010C,020C, Met One, Grants Pass, OR)
215 and THC concentration, C , by a Flame Ionization detector (51i-LT, Thermo Scientific, MA). WCS is maintained by
216 the Santa Barbara County Air Pollution Control District. Daily instrument calibration occurs after midnight, rendering
217 C unavailable 00:50 to 02:09 local time, LT. WCS was improved significantly in 2008 from 1-hour to 1-minute time
218 resolution, which allowed for higher values of C and u due to the shorter averaging times. Data analysis uses custom
219 routines as well as standard routines and functions in MATLAB (MathWorks, MA).

220
221 First, WCS data were quality controlled to remove all values of C during the daily calibration, as well as to interpolate
222 neighboring values that were unrealistically low, i.e., C less than 1.6 ppm in the 1990s and 1.85 ppm in the 2000s.
223 Data since 2008 were smoothed by nearest-neighbor averaging, yielding 3-minute time resolution. Data prior to 2008
224 were hourly and were not smoothed. Wind data were nearest-neighbor averaged after decomposing into north and east
225 components, followed by recalculation of u and θ .

226

227 **2.2 *In situ* marine surveys**

228 Offshore *in situ* survey data were collected by the *F/V Double Bogey*, a 12-m, 9-ton, fishing vessel with a near
229 waterline deck (~0.2 m) and low overall profile (cabin at ~2.2 m). A sonic anemometer (VMT700, Vaisala) was
230 mounted on a 6.5-m tall, 5-cm (2") diameter aluminum mast and measured 3D winds. Continuous, CH₄ and CO₂ data
231 were collected 5 Hz by a Cavity Enhanced Absorption Spectroscopy (CEAS) analyzer (FGGA, LGR Inc., San Jose,
232 CA). Vessel location and time were from a Global Positioning System (GPS) at 1 Hz (19VX HVS, Garmin, KS). CH₄
233 and CO₂ calibration with a greenhouse gas air calibration standard (CH₄: 1.981 ppmv; CO₂: 404 ppmv, Scott Marin,
234 CA, purchased 2015, Sigma Aldrich, St Louis, MO).

235

236 Data are real time integrated and visualized in Google Earth on a portable computer (Spectre360, HP) using custom
237 software, written in MATLAB (MathWorks, MA) for AutoMOBILE trace Gas (AMOG) Surveyor, described elsewhere
238 (Leifer, Melton, Fischer, et al., 2018; Leifer, Melton, Manish, & Leen, 2014; Leifer, Melton, Tratt, et al., 2018; Leifer
239 et al., 2016). Real-time visualization facilitates adaptive surveys, wherein the survey route is modified based on real-
240 time data to improve outcomes (Thompson et al., 2015) - in this case to facilitate plume tracking and to ensure transects
241 were near orthogonal to the wind.

242

243 Accurate, absolute winds are calculated from relative winds after accounting for vessel motion and filtering for non-
244 physical velocity changes due to GPS uncertainty (Leifer, Melton, Fischer, et al., 2018). Filtering removes transient
245 winds that are not relevant to plume transport. The filter interpolates GPS positions flagged as unrealistic.

246
247 Whole air samples were collected in evacuated 2-liter stainless steel canisters, which were filled gently over ~1 minute
248 from ~1 m above the sea surface. The filled canisters were analyzed in the Rowland/Blake laboratory at the University
249 of California, Irvine for carbon monoxide, CO, CH₄, and C₂-C₇ organic compounds. Samples were analysed by a gas
250 chromatography multi-column/detector analytical system utilizing flame ionization detection.

251

252 **2.3 Seep plume emissions model**

253 The plume inversion model is a three-step process (Leifer, Melton, Fischer, et al., 2018; Leifer, Melton, Tratt, et al.,
254 2018; Leifer et al., 2016). Emissions from focused seep areas were derived from offshore data by first fitting Gaussian
255 function(s) to orthogonal transect C' data, termed the data model. C' is relative to C outside the plume, derived by
256 linear interpolation across the plume transect. The data model is derived by error minimization using a least-squares
257 linear-regression analysis (Curve fitting toolbox, MathWorks, MA). Next, the Gaussian plume model (**Eqn. S1; Supp.**
258 **Figs. S1; S2**) is fit to the data model. Transect data are collected close to orthogonal to the wind direction and are
259 projected in the wind direction onto an orthogonal plane. See Leifer, Melton, Tratt, et al. (2018) for a validation study
260 of the plume inversion model by comparison with remote sensing-derived emissions (which are largely insensitive to
261 transport). The study found *in situ* and remote-sensing derived emissions agreed within 11%.

262

263 **2.4 Seep field emissions model**

264 The inversion model is based on gridding the seep field into numerous small additive Gaussian plumes that represent
265 the area emissions and was written in MATLAB (MathWorks, MA). This assumes that each sea-surface grid cell
266 contributes a Gaussian plume, an assumption that was tested with offshore survey data downwind of several active
267 seep areas.

268

269 The definition of area versus point source depends on the relevant length scales – an area source is well approximated
270 as a point-source plume if sufficiently downwind (far field), where the distance for “sufficiently downwind” depends
271 on the area source dimensions and meteorological conditions. Whereas WCS is near field for the entire seep field
272 plume, it is far field for the small plumes from each grid cell.

273

274 The area source was based on a Sept. 2005 sonar survey sonar return, ω , map (**Fig. 1**), see Leifer et al. (2010) for
275 sonar survey details. Simulations used sonar data gridded at a hybrid 22/56-m in a UTM coordinate system, with origin
276 at WCS. Specifically, gaps in the 22-m map were filled from the 56-m map (**Supp. Fig. S3**). The probability
277 distribution of ω was used to identify the noise level (**Supp. Fig. S4**) as in Leifer et al. (2010).

278

279 The model calculates a Gaussian plume for E_{ij} for grid cell i and j , for each grid cell with ω above noise. $C'_{Sim}(x, y)_{i,j}$
280 are calculated for the observed $u(\theta)$ in wind direction θ and a typical Santa Barbara channel boundary layer, $BL=250$
281 m. The initial E_{ij} is by scaling such that the integrated sonar return ($\int \omega(x,y)$) scales to $E_A=1.5 \times 10^5 \text{ m}^3 \text{ dy}^{-1}$, i.e., E_B from
282 Hornafius et al. (1999). The Gaussian plume is calculated in a Cartesian coordinate system (**Supp. Fig. S5A**), rotated
283 to θ , and the interpolated linearly to double the spatial resolution. Then, the rotated plume is regridded to UTM
284 coordinates using the `ffgrid.m` function (**Supp. Fig. S5B**). Interpolation removes gaps in the regridded plume map.
285 Then, the regridded plume is renormalized to ensure total mass is conserved before and after these operations. Rotated
286 regridded plumes are translated to the seep field grid and added, yielding $C'_{Sim}(x, y)$, the simulated seep field plume
287 anomaly (**Supp. Fig. S5C**).

288

289 The model scans θ for the seep directions ($110^\circ < \theta < 330^\circ$) and calculates the simulated plume anomaly, $C'_{Sim}(\theta)$ at
290 WCS, which is compared with the observed $C'_{Obs}(\theta)$ at WCS. Hereafter, C_{Obs} and C_{Sim} and their anomalies refer to
291 values at WCS. $C'_{Obs}(\theta)$ is defined:

$$292 \quad C'_{Obs}(\theta) = C_{Obs}(\theta) - \min(C_{Obs}(\theta)) \quad (1)$$

293 with the minimum typically from the west in a direction with no known seepage. Specifically, $C'_{Obs}(\theta)$ was calculated
294 by subtracting the minimum in the annualized observed $C'_{Obs}(t, \theta)$ each year, t , after applying a 7-year running
295 average.

296

297 Emissions from suburban communities, light industry, and commercial centers enhance $C'_{Obs}(\theta)$ for the north to east
298 ($\sim 350\text{-}70^\circ$) sectors. Removal of these terrestrial emissions was by fitting a Gaussian function to $C'_{Obs}(\theta)$ for
299 $330^\circ < \theta < 30^\circ$ with the residual yielding $C'_{Obs}(\theta)$. This only affected $C'_{Obs}(\theta)$ for overlapping directions corresponding
300 to the fields' eastern edge.

301

302 Simulations were run at angular resolutions of 2° . Higher angular resolution produced small artifacts for the 22/56-m
303 sonar grid while the 11-m sonar grid was overly sparse due to the distance between sonar tracks (**Supp. Fig. S3**).

304

305 The source map is ω in units of decibels, whereas emissions are in units of moles $\text{m}^{-2} \text{ s}^{-2}$. Given that the relationship
306 between ω and bubble density (emissions) is complex and non-linear (Leifer et al., 2017), there is poor agreement
307 between $C'_{Sim}(\theta)$ and $C'_{Obs}(\theta)$. Thus, a correction function, $K(\theta)$, is applied to emissions for each grid, $E(i,j)$, along
308 each θ and the model rerun. $K(\theta)$ is defined,

$$309 \quad K(\theta) = C'_{Obs}(\theta) / C'_{Sim}(\theta) \quad (2)$$

310 Initially, $K=1$, but in subsequent iterations, $K(\theta)$ is scaled as in **Eqn. 2** to adjust E_A in cells along θ . Because $K(\theta)$
311 weights closer seeps more than more distant seeps, a distance-varying correction function, $K(r, \theta)$, was calculated such
312 that,

$$313 \int_{r=0}^{r=\infty} E_A(r, \theta) = \int_{r=0}^{r=\infty} K(r, \theta) E_A(r, \theta) dr \quad (3)$$

314 where r is distance from WCS. Simulations that shifted WCS northwards showed E_A varied nearly linearly with
315 distance. Accounting for off-axis plume contributions requires several iterations to achieve *Convergence*, which was
316 defined,

$$317 \textit{Convergence} = \frac{\sum C'_{Sim}(\theta) \sum C'_{Obs}(\theta)}{\sum C'_{Obs}(\theta)} \quad (4)$$

318 Iterations continued to *Convergence* of 1% or better – typically 4 to 5 iterations. Simulations suggest wind veering,
319 ψ , was important, which was implemented by calculating $C'(\theta)$ and assigning it to $C'(\theta + \psi)$.

320

321 **3 Results**

322 **3.1 Offshore *in situ* surveys**

323 An offshore COP seep field survey measured *in situ* C_{CH_4} and u on 28 May 2016. Data were collected from the Santa
324 Barbara harbor (~7.5 km east of the seep field, **Fig. 2A**; **Supp. Fig. S6**) to offshore Naples, several kilometers west
325 of the seep field. Overall winds were easterly with an onshore component near Campus Point and a broad (6-km wide)
326 offshore flow west of COP that shifts to along coast near Naples (**Fig. 2A, white arrows**). Observed winds veered
327 ~10° from east to the west sides of the seep field, roughly comparable to the shift in coastline orientation.

328

329 Plumes are apparent downwind of major seeps, with the largest plume associated with the Trilogy Seep (**Fig 2B**).
330 Strong plumes also are evident downwind of the La Goleta Seep and Patch Seep. Notably, the Seep Tent Seep plume
331 was very weak. The Seep Tent Seep was the dominant seep area in the COP seep field from its appearance in June
332 1973 (Boles, Clark, Leifer, & Washburn, 2001) until recent years.

333

334 Additionally, the offshore survey identified focused plumes from beyond the extent of the seep field's 2005-sonar
335 map. Specifically in the Goleta Bay, which has been noted (Jordan et al., 2020), and offshore Haskell and Sands
336 Beaches, areas of abandoned oil wells, and off Naples Point (**Fig. 2A, red arrow**).

337

338 Plume alkane C' were determined by the difference between two “background” air samples collected immediately
339 outside the plume and three Trilogy Seep plume air samples. CH_4 was 88.5% of THC, with ethane, propane, and
340 butane at 3.1%, 4.2%, and 2.76%, respectively, with pentane, hexane, and heptane at 1.11, 0.13, and 0.04%,
341 respectively (**Table 1**). THC molecular weight is 19.6 g mole⁻¹ based on a composition weighting. Branched alkanes

342 were detected, with 2-methylpentane and 3-methylpentane comprising 0.21%, each, as well as simple aromatics, e.g.,
343 benzene and toluene, with concentrations of 0.044 and 0.100 ppm, respectively.

344
345 The observed wet gas fraction, $\sum_{n=2}^5 C_n / \sum_{n=1}^5 C_n$ was 0.11 indicating a thermogenic origin - greater than 0.05
346 (Abrams, 2017) - and thus derived from marine organic materials. Although the olefins ethene and ethyne were
347 detectable at 0.02% and 0.004%, respectively, butene was not detected. These olefins primarily derive from microbial
348 processes (Abrams, 2017), thus, the ethane/ethyne ratio of 6200 also strongly indicates a thermogenic source (Bernard
349 et al., 2001). Atmospheric CO₂ was elevated by 12 ppm. Given that CO₂ completely dissolves from bubbles well
350 before reaching the sea surface (Clark et al., 2010), this demonstrates efficient vertical transport of dissolved seep
351 gases to the sea surface.

352
353 Plumes for the Trilogy Seeps, La Goleta Seep, and Seep Tent Seep were inverse modeled to derive emissions for each
354 plume. For the Trilogy Seeps, the average u across the plume was 5.9 m s⁻¹, insolation was full sun, and the source
355 height was set at 25 m based on Trilogy's atmospheric plume being buoyant. Model surface concentrations for Trilogy
356 B plume are shown in **Fig 2A**. The other two seeps are far less intense and used a 1-m source height.

357
358 E for Trilogy A was 1.28 Gg CH₄ yr⁻¹ (5600 m³ CH₄ dy⁻¹), whereas Trilogy B and C contributed 0.06 and 0.07 Gg
359 CH₄ yr⁻¹, respectively, for a total of 6200 CH₄ m³ dy⁻¹. Note, plume origins and the sonar seep bubble plume locations
360 do not precisely match because the sonar map is for near the seabed, and currents deflect the bubble surfacing location,
361 up to ~40 m. La Goleta Seep released 4000 m³ CH₄ dy⁻¹ and the Seep Tent Seep released 310 m³ CH₄ day⁻¹ with
362 almost no surface bubble expression. For comparison, Clark et al. (2010) used a flux buoy, which measures near
363 surface bubble fluxes, and found Trilogy Seep emissions of 5500 and 4200 m³ THC dy⁻¹ and 930 m³ THC day⁻¹ for
364 La Goleta Seep in 2005 and 5700 m³ THC dy⁻¹ for the Seep Tent Seep in 2002. During the cruise, surface bubble
365 plumes were not observed for the Seep Tent Seep, although its bubble plume had been a perennial and dominant
366 feature since its appearance. Note, Clark et al. (2010) reported THC in near sea surface bubbles was 91% CH₄.

367

368 **3.2 West Campus Station**

369 **3.2.1 Temporal trends**

370 WCS is 500 m from the coast (to the southwest) at 11-m altitude and 850 m almost due south to the 11-m altitude
371 bluffs of Coal Oil Point (**Fig. 1**). Terrain slopes gently towards the coast to the southwest and towards a lagoon to the
372 south-southeast, rising again to the southeast to the COP bluffs. This flat relief likely has small to negligible effect on
373 wind speed and direction, although differential land-ocean heating could influence winds. Wind veering for the coast
374 to the east of COP is likely due to the orientation of the coastline and bluffs.

375
376 The WCS improvements in 2008 (**Fig. 3-dashed line**) allowed far higher values of C and u (**Supp. Fig. S7A,7B**).
377 Comparison of the probability distributions of u and C , $\phi(u)$ and $\phi(C)$, respectively, before and after the upgrade did

378 not suggest biases were introduced (**Supp. Fig. S7C,7D**). Specifically, changes in the average and median values and
379 in the baseline after 2008 were from better measurement of higher value events (gusts and short positive C anomalies).
380

381 Significant daily, seasonal, and interannual variations are apparent in the day-averaged u and C (**Fig. 3**). The calmest
382 season is late summer to fall, whereas spring is the windiest and most variable due to synoptic systems (**Fig. 3A**).
383 Winds have strengthened since a minimum in 1995-1996, moreso for the seep directions with stronger winds becoming
384 more frequent and moreso for summer than winter (**Supp. Figs. S8, S9**).
385

386 Trends in C reflect trends in both seep field emissions and ambient C . C is higher in fall and spring (**Fig. 3B**). Given
387 that stronger winds decrease C through dilution, this suggests the seasonal variation in C underestimates the seasonal
388 variation in emissions. Several studies have shown increased emissions under higher wave regimes (storminess),
389 reviewed in Leifer (2019) and proposed from wave pumping. Storms increase evasion from higher wave turbulence
390 and breaking-wave bubbles, which sparge dissolved CH_4 and other trace gases down to the seabed in shallow (<100
391 m) waters (Shakhova, Semiletov, Salyuk, et al., 2010). Note, u , θ , and C' correlate with time of day. For example,
392 north generally reflects weak, offshore nocturnal winds with no seep contribution.
393

394 **3.2.2 Spatial heterogeneity**

395 Calculating the angular-resolved average C , $C_{ave}(\theta)$, for the complete dataset with respect to θ shows the highest C
396 from the main seep field direction (155-250°, **Fig. 4**). For the seep directions, $C_{ave}(\theta)$ was poorly fit by a single
397 Gaussian function but well fit ($R^2=0.997$) by two Gaussian functions with peaks at 178° and 198° corresponding to
398 the Seep Tent and Trilogy Seeps' directions, respectively (**Fig. 4A, 4B**). Notably, the fit residual showed a linear
399 increasing trend, $dC_{ave}(\theta)/d\theta$, of 0.17 ppb degree⁻¹ from 180 to 210° (**Supp. Fig. S9B**) consistent with evasion from
400 a dissolved downcurrent plume that drifts west-northwest along the coast (Leifer, 2019).
401

402 The average C anomaly, $C'_{ave}(\theta)$, was calculated from the average of $C_{Obs}(\theta)$ after **Eqn. 1** with terrestrial
403 anthropogenic sources to from the north to northeast removed. The minimum in $C_{Obs}(\theta)$ was at 270°, a direction with
404 no mapped seepage that also is at the dissolved plume's approximate shoreward edge. **Fig. 4A** shows $C_{Obs}(\theta)$ before
405 removal of terrestrial emissions, which do not overlap in any significant manner with seep field emissions.
406

407 There is a strong, focused peak in $C_{max}(\theta)$ at $\theta \sim 190^\circ$, close to the Seep Tent Seep direction (**Fig. 4E, 4F**), which is
408 fairly isolated on the Ellwood Trend (**Fig. 1**). This peak also is close to the direction of Tonya Seep on the inshore
409 seep trend and to the small, unnamed area of seepage to the west of Trilogy Seep along the Red Mountain Fault trend.
410 The θ -resolved maximum $C(\theta)$, $C_{max}(\theta)$, remains elevated through $\sim 270^\circ$, far west of the $C_{ave}(\theta)$ peak at $\sim 200^\circ$.
411 This strongly suggests that the seep field extends further to the west-northwest than current maps. These data cannot
412 be explained by dissolved plume outgassing, which would affect $C_{ave}(\theta)$ but not $C_{max}(\theta)$.
413

414 $C(\theta)$ enhancements for non-seep directions (**Fig. 4A,4B**) show a peak at $\sim 35^\circ$, corresponding to the direction of a
415 commercial center amid suburban development. This could result from terrestrial seepage and natural gas pipeline
416 leakage and/or THC emissions from communities and traffic.

417
418 Neglecting the synoptic system, topographic forcing from the east-west Santa Ynez range means that prevailing winds
419 are westerlies and are the strongest (**Fig. 4C, 4D**). North winds ($320-15^\circ$) largely are weak as are winds from due
420 south; however, the sea breeze strengthens winds rapidly away from due south. θ peaks in the maximum winds (1-
421 minute sustained), $u_{max}(\theta)$, correspond to the west and east peaks in $u_{ave}(\theta)$ with strengths to 16 m s^{-1} . Interestingly,
422 there also are strong north ($0-30^\circ$) winds or downslope flow, termed sundowner winds, a highly localized and
423 infrequent phenomenon. The overlap of $u_{med}(\theta)$ and $u_{ave}(\theta)$ shows winds largely are normally distributed.

424
425 The median C , $C_{med}(\theta)$, and average C , $C_{ave}(\theta)$, have similar shapes, albeit with lower values at all θ (**Fig. 4A**),
426 indicating C is not normally distributed. This is shown in the wind direction-resolved wind speed probability
427 distribution, $\phi(\theta, u)$ (**Fig. 5A**), defined such that

$$428 \int \phi(\theta, u) du = 1, \quad \int \phi(\theta, C) dC = 1 \quad (5)$$

429 $\phi(\theta, u)$ is very narrow (y-axis) for the northeast ($\sim 45^\circ$) where winds are largely weak and broad for the east-southeast
430 ($70-135^\circ$) and the prevailing westerlies ($250-280^\circ$). The east-southeast distribution skews to the south (stronger winds
431 extend further from the south - offshore), whereas the prevailing westerly wind distribution skews to the northeast (as
432 does the coastline).

433
434 In the seep direction, $\phi(C, \theta)$ extends to much higher values than from non-seep directions (**Fig. 5B**). $\phi(C, \theta)$ is
435 asymmetric with θ extending further to the west than the seep field extent (240°) and then decreasing more abruptly
436 than the decrease to the east. This asymmetry is expected given the seep field's asymmetric orientation relative to
437 WCS (eastern seepage is more distant). Emissions beyond the field's mapped western edge arise from downcurrent
438 plume outgassing and potentially contributions from unmapped seeps.

439
440 **3.2.3 Seep field diurnal emissions cycle**

441 C and u for the seep field direction, u_{seep} , and C_{seep} , respectively, follow diurnal patterns that are not the same as the
442 overall diurnal pattern due to the wind direction constraint and because C_{seep} depends on u_{seep} . The dependency arises
443 because higher u dilutes emissions, decreasing C , but higher u also increases dissolved plume evasion and bubble-
444 mediated emissions from higher swell (after a delay for wave buildup). Diurnal winds in coastal regions feature a shift
445 between weak nocturnal offshore winds that veer to onshore winds in the morning - the sea breeze circulation. This
446 was explored in time and direction segregated u and C and seep direction averaged u_{seep} , and C_{seep} for $90-270^\circ$ (**Fig.**
447 **6**). Data were segregated by θ for pre- and post-2008 (when station improvements facilitated better wind
448 characterization, particularly for night winds, which are seldom from the seep field direction, see **Supp. Fig. S10** for

449 1991-2007). $u(\theta,t)$ and $C(\theta,t)$ were 2D Gaussian kernel smoothed with a 1-bin standard deviation (contours based on
450 a 3 bin standard deviation) by the `imgaussfilt.m` algorithm (MATLAB, MathWorks, MA) after interpolating the
451 calibration data gap 24:00-01:00.

452
453 Early morning (01:00–03:00) u_{seep} are stronger because typical nocturnal winds are northerlies (land breeze), coming
454 from the south largely during storms. These are accompanied by elevated C_{seep} implying greater emissions despite
455 enhanced dilution from stronger winds. The minimum in both u_{seep} and C_{seep} occur in the early morning (04:00-08:00),
456 with both increasing slightly through midday (~12:00). C_{seep} follows an afternoon trend of an overall decrease to a
457 minimum at ~20:00 before increasing into the late evening.

458
459 Underlying these trends are complex temporal spatial patterns. u for the north to northeast reaches a maximum around
460 noon and peak around 16:00; while C for northeast to east is low in the morning reaching a peak to the east in the
461 afternoon and likely reflects terrestrial sources. This pattern in $C(t,\theta)$ extends to nearly 130° . Beyond the seep field's
462 western edge, u is elevated from the prevailing direction (270°), with C elevated throughout the morning. There also
463 is a short-lived peak in u around noon at $\sim 300^\circ$, which corresponds to a short-lived depressed C . These could be
464 consistent with wave development time, transport time, and sparging of the downcurrent plume; however,
465 interpretation based on these patterns largely is speculative.

466

467 3.3 Overall seep field emissions

468 3.3.1 Overall emissions

469 Average atmospheric emissions, E_A , for 1990-2020 were derived by an iterative Gaussian plume model, initialized
470 with the 2005 sonar map (**Fig. 7A**). An emissions sensitivity study on the effect of grid resolution was conducted for
471 resolutions from 11 to 225 m and a 22/56-m hybrid grid (**Fig. S3**). Simulations used moderate insolation to derive the
472 turbulence parameters and stability class, a 250-m BL , a typical Santa Barbara Channel marine values (Edinger, 1959;
473 Rahn, Parish, & Leon, 2017), and 2° angular resolution (Hanna et al., 1982). Simulations were run iteratively until
474 convergence, typically within 5 iterations (**Supp. Fig. S11**). Sensitivity studies found the distance weighting function,
475 $K(r,\theta)$, was linear (**Supp. Fig. S12**).

476

477 Simulations could not reproduce observations in the Platform Holly direction ($\theta=238^\circ$). Thus, a source was added for
478 the platform area, which improved simulation-observational agreement in this wind direction. Since significant seep
479 bubbles plumes generally are not observed in the platform's vicinity, these emissions could arise from incomplete
480 combustion from flaring.

481

482 The model-derived, E_A , for 1990-2020 was $83,500 \text{ m}^3 \text{ dy}^{-1}$ (**Fig. 7**). Using a composition-weighted molecular mass of
483 19.6 g mole^{-1} implies $27 \text{ Gg THC yr}^{-1}$. Atmospheric seep gas is 88.5% CH_4 , implying $19 \text{ Gg CH}_4 \text{ yr}^{-1}$ seep emissions
484 (**Table 1**). Given that CH_4 is 73% of THC, non-methane hydrocarbon (NMHC: $\text{C}_2\text{-C}_7$) emissions are $9,500 \text{ m}^3 \text{ dy}^{-1}$

485 and Reactive Organic Carbon (ROC) gases emissions of 6.0 Gg yr^{-1} - ROC are organic species excluding CH_4
486 including alkanes and aromatic compounds. For reference, Santa Barbara County 2018 ROC emissions were ~ 27 tons
487 dy^{-1} (9.9 Gg yr^{-1}) (ourair.org/emissions-inventory, SBAPCD). The largest NMHC was propane with emissions of 3510
488 $\text{m}^3 \text{ dy}^{-1}$, followed by ethane at $2590 \text{ m}^3 \text{ dy}^{-1}$. The NMHC components of THC are conservative (do not react
489 significantly) on the typical the transport time from the seep field to WCS (20-30 minutes).

490
491 Seabed emissions, E_B , are necessarily significantly greater than E_A as E_A misses the fraction of emissions that remain
492 in the water column, E_W , at least in the field's near downcurrent. There are two notes, the model E_A includes evasion
493 from the dissolved plume in the area covered by the seep field sonar map. Secondly, the model does not include E_A
494 from the dissolved fraction that evades beyond the seep field extent. For the seep field area and near downcurrent area,
495 Clark et al. (2000) estimated a 50:50 air/water partitioning, implying seabed emissions, E_B , 1990-2020 of $167,000 \text{ m}^3$
496 dy^{-1} or 54 Gg yr^{-1} . A comparison of E_A versus ω showed a very steep increase with ω for $E_A = 1-10 \text{ g s}^{-1} \text{ m}^{-2}$ with
497 rollover at $\omega \sim 0.022$ (Supp. Fig. S13).

498
499 Insights were provided by how the model partitioned emissions between different seep areas. Particularly notable is
500 the model's treatment of the Trilogy Seep area - the second strongest seep area after the Seep Tent Seep over 1990-
501 2020. The model re-assigned Trilogy Seep emissions to seepage to the west, representing Trilogy Seep emissions as
502 unrealistically weaker than other, smaller seeps, such as IV Super Seep. One likely contributor to this re-assignment
503 is wind veering. Also suggesting wind veering is the model's assignment of strong emissions to the field's eastern and
504 western edges despite weak sonar returns. In a comparison of the Seep Tent Seep and La Goleta Seep areas, the model
505 emphasized the Seep Tent Seep whereas La Goleta Seep emissions were shifted to inshore seepage. This re-
506 partitioning was greatly reduced for a $+10^\circ$ wind veer, which also lessened the strengthening of emissions from the
507 field's western edge relative to sonar (Supp. Fig. S14). Given the lack of field data between the seep field and WCS
508 on wind veering, further wind veering analysis was not conducted.

509

510 3.3.2 Seep field sector emissions

511 To investigate sub-field scale emissions, the seep field was segregated into three sectors: inshore, offshore east, and
512 offshore west (Fig. 1). Based on integrating sonar return, ω , the inshore seepage contributes 40% of the field's ω with
513 the offshore seep trend split between 9% for the west and 51% for the east. Supporting this comparison is the similarity
514 in the normalized sonar return probability distribution, $\phi_n(\omega)$, for the inshore seeps and offshore east seeps (Fig. 8). In
515 contrast, $\phi_n(\omega)$ for the offshore west seepage differed dramatically despite the similarity in geology along the anticline
516 underlying the offshore seep trend (Leifer et al., 2010). This likely results in part from the interaction between
517 migration and production from Platform Holly. Although the normalized atmospheric emissions probability
518 distribution, $\phi_n(E_A)$, for the inshore and offshore seeps are similar over most of the range (except the weakest, $E_A < 0.02$
519 g s^{-1}), significant differences are evident between offshore east and west seepage. Offshore east seepage is more
520 dispersed and favors weaker seepage compared to offshore west seepage and compared to $\phi_n(\omega)$.

521
522 The weakest seepage ($\omega < 0.02$) contributes negligibly to overall sonar return and had no notable inshore-offshore $\phi_n(\omega)$
523 difference. The largest difference is between the strongest seepage ($\omega > 0.5$) for the inshore and offshore seeps.
524 Specifically, there is a strong peak at $\omega \sim 0.45$ and nothing stronger for the inshore seeps, whereas offshore $\phi_n(\omega)$
525 continued to $\omega \sim 0.7$. The E_A probability distribution, $\phi_n(E_A)$, for the strongest inshore seepage was similar to $\phi_n(E_A)$ for
526 strong offshore seepage. However, this masked a significant east-west offshore seepage difference. Specifically,
527 $\phi_n(E_A)$ for strong seepage was reduced far more for offshore east seepage than offshore west seepage, and the reverse
528 for weak seepage.

529
530 These distributions suggest that controlling geological structures (fractures, fault damage zones, and chimneys in the
531 capping Sisquoc Formation) are the same for inshore seepage and offshore east seepage, with the primary difference
532 for the strongest seepage in these two sectors which are of similar strength – the inshore Trilogy Seeps provide focused
533 emissions, whereas the offshore east La Goleta Seeps are comparatively dispersed and far oilier.

534
535 Although, ω is not E_A , E_A followed the 40:60 partition in ω between inshore and offshore seepage. Interestingly, the
536 E_A partitioning between the offshore east and offshore west differed significantly from sonar partitioning with 21% of
537 E_A from offshore west and 38% from offshore east. This greatly accentuated the E_A Seep Tent Seep area. In part, this
538 arises from a diurnal cycle bias – WCS observes the offshore west seeps for afternoon/evening westerly winds, which
539 are stronger, whereas WCS observes the offshore east seeps when winds are weaker, earlier in the day (**Fig. 6B**).
540 Winds increase bubble emissions from wave hydrostatic pumping and dissolved gas evasion. Also potentially
541 contributing is saturation of ω at very high bubble-density bubble plumes, such as the Seep Tent Seep and Trilogy
542 Seep (Leifer et al., 2017). Saturation would imply an under-estimate of ω for the strongest seep area emissions which
543 are for the west offshore seepage, altering the west: east ω ratio (9%:51%).

544

545 **3.3.3 Uncertainty and emissions sensitivity**

546 Given the number of sources with poorly characterized variability, uncertainty is best assessed by Monte Carlo
547 simulations; however, this was unfeasible due to the simulations' computational demands. Thus, emissions uncertainty
548 was investigated by sensitivity studies (**Fig. 9**). Where data were available, uncertainty due to a specific parameter
549 was estimated from the data. Specific parameters studied included sonar resolution, angular resolution, $\delta\theta$, wind speed,
550 u , concentration anomaly, C' , boundary layer height, BL , wind veering, ψ , spatial northing offset, Y , and the inshore
551 and offshore seepage partitioning, ζ . Sensitivity study details are presented in **Supp. Sec. S7.4**.

552
553 The contribution to uncertainty from $\delta\theta$, C' , ψ , and spatial offsets within the seep trends were minimal – just a few
554 percent or less. Moderate uncertainty was identified for BL and ζ . For example, for BL ranging from 150 to 350 m,
555 mean E_A uncertainty was 6%. Although u has strong sensitivity, combined with BL it does not as u counters BL –

556 lower u corresponds to higher BL . There still is uncertainty, though in the value of BL , which is not measured.
557 Assessing uncertainty in ζ was more challenging as there is no verification data on variability in the E_A partitioning
558 between the inshore and offshore seep trends. The mean E_A uncertainty for $-50\% < \zeta < 50\%$ is 11.5% from a polynomial
559 fit. Still, the consistency in seepage location between sonar surveys spanning decades (Leifer, 2019) suggests only
560 modest changes in ζ over the multi-decade time period of model averaging. Total uncertainty was taken as 15% based
561 on the sum of uncertainty in BL and ζ , each averaged to the nearest 5%.

562

563 3.4 Ellwood Field emissions

564 $C(\theta)$ increases to the northeast with a peak at $290\text{-}320^\circ$ corresponding to the direction towards abandoned wells off
565 Haskell Beach (**Fig. 10**). Emissions from this area – either from natural seepage or leaking wells – were noted in the
566 offshore survey data near Haskell Beach (**Fig. 2A**). Additionally, $C_{max}(\theta)$ shows a 22-ppm peak in in this direction
567 well above $C_{ave}(\theta)$ (**Fig. 4F**), consistent with transient releases from natural seep and/or abandoned well emissions.

568

569 Ellwood field production continued through the 1970s with wells drilled into the geological structures that allowed
570 oil accumulation (Olson, 1983); including faults that provide migration pathways (Leifer et al., 2010). There are many
571 abandoned wells from these oil fields and from others fields on the Goleta Plains, beaches, and shallow near-coastal
572 waters to the west-northwest of WCS (offshore Haskell Beach and onshore around Naples Point). Currently, active
573 wells only are found at the La Goleta Gas field (a natural gas storage field), east of WCS.

574

575 Faults associated with these anticlines provide migration pathways and are approximately aligned with the coast in a
576 series of roughly parallel faults extending onshore (Minor et al., 2009). The onshore/coastal Ellwood field (northwest
577 of the South Ellwood field) sources from the primarily sandstone Vaqueros Formation (Olson, 1983), whose main
578 trap is an anticline at the western edge of the North Branch Western More Ranch Fault (NBWMRF). Offshore seepage
579 tracks some of these faults, e.g., the Isla Vista Fault trend corresponds to an offshore seep trend in Goleta Bay that
580 includes the Goleta Pier Seep, whereas wells follow the NBWMRF trend offshore of Haskell Beach.

581

582 4 Discussion

583 4.1 Atmospheric seep field observations

584 4.1.1. Air quality station

585 A range of approaches are available to evaluate marine seepage CH_4 emissions: *in situ* approaches including direct
586 capture (Leifer, 2015; Washburn, Johnson, Gotschalk, & Eglund, 2001), fluid flow measurements (Leifer & Boles,
587 2005), video (Leifer, 2015), and remote sensing approaches that include active acoustics, i.e., sonar (Hornafius et al.,
588 1999), dissolved *in situ* (Marinero et al., 2006), and passive acoustics (Wiggins et al., 2015). Remote sensing is the

589 best approach for long-term monitoring to capture shifts in emissions between vents. To date, only sonar remote
590 sensing has provided quantitative seep plume (seabed) emissions. Notably, sonar ranges are up to a few hundred
591 meters, far less than the size scales of many seep fields, while high power-demands typically require a cabled
592 observatory for long-term observations.

593
594 This study demonstrated that air quality station data can provide the long-term continuous data needed to capture
595 seasonal variations including emissions during storms and transient events, which field campaigns likely miss. For
596 example, sonar surveys tend to occur during summer when seas are calmer and more predictable and when seepage is
597 weakest (**Fig. 3**); however, not during storms when emissions likely are enhanced.

598
599 The approach derived atmospheric trace gas emissions for a dispersed area source constrained by sonar seepage maps
600 from long-term air quality and meteorology data. This approach can be extended to terrestrial seepage if the source
601 can be constrained spatially (due to geology); although nearby anthropogenic sources may complicate emissions
602 assessments. Other terrestrial sources such as landfills, O&G production fields, or industrial sites – if spatially
603 constrained – could be addressed by this approach, particularly if isolated from other confounding sources. The use
604 of cavity enhanced absorption spectrometers that can speciate gases like CH₄ and C₂H₆ could enable discrimination
605 some confounding sources as well as better characterization of emissions. Although an onshore station can address
606 nearshore seepage, further offshore seepage could be addressed by a moored station. Moored stations also could
607 include *in situ* aqueous chemical sensors, current measurements.

608

609 **4.1.2 *In situ* atmospheric surface surveys**

610 Atmospheric emissions were assessed for three seep areas - zone of focused seepage - by an atmospheric *in situ* survey
611 approach wherein downwind data are collected orthogonal to the wind direction in a transect that spans the plume
612 (background to background on the plume's edges). This approach was developed for terrestrial sources (Leifer,
613 Melton, Tratt, et al., 2018) yet remains unused for offshore marine seepage, which often are area sources. In this study,
614 this was addressed by gridding the area source and treating each grid as a far-field point source. Gaussian plume
615 inversion requires distant source(s), i.e., far field. Surveys of three strong seep areas all were well characterized by the
616 Gaussian plume model.

617
618 One advantage of atmospheric surveys is rapidity - a single transect of a few minutes is sufficient to derive emissions
619 for a seep area. In comparison, a flux buoy survey can require many hours to a day (Clark et al., 2010), during which
620 forcing factors (waves, tides, etc.) change significantly. Also rapid are seep area sonar surveys (Wilson, Leifer, &
621 Maillard, 2015) allowing a combined sonar and atmospheric survey to repeat characterize emissions and sea-air
622 partitioning within a few hours. With respect to the entire COP seep field, whereas a sonar survey requires two to
623 three days (Leifer et al., 2010), a downwind atmospheric survey is far more rapid, requiring perhaps an hour. This
624 allows repeat field emissions measurements over a tidal cycle.

625

626 **4.2 Seep field emissions**

627 **4.2.1 Total emissions**

628 To date, only two estimates of COP seep field seabed emissions, E_B , have been published. Hornafius et al. (1999)
629 estimated $E_B=1.5 \times 10^5 \text{ m}^3 \text{ dy}^{-1}$ (64 Gg yr⁻¹) based on sonar surveys covering 18 km² from Nov. 1994 – Sep. 1996,
630 collected during the summer to late fall seasons. This value excluded Seep Tent collection. A 4.1 km² sonar survey in
631 Aug.-Sep. 2016 estimated $E_B=24,000 \text{ m}^3 \text{ dy}^{-1}$ (Padilla, Loranger, Kinnaman, Valentine, & Weber, 2019), significantly
632 lower, which in part arises from field subsampling, but also could arise from long-term changes; however, neither
633 study addressed temporal variability. The sonar surveys occurred in summer and fall when seepage activity is at a
634 minimum, whereas winter and early spring feature much higher activity associated with large transient events and
635 storms (Bradley et al., 2010).

636

637 Hornafius et al. (1999) used an engineered bubble plume to calibrate emissions, an approach also used in Leifer et al.
638 (2017). Due to technology limitations at the time, the strongest seepage was clipped or saturated, i.e., underestimated,
639 and the survey did not cover shallow seepage. Thus, the Hornafius et al. (1999) emissions estimate is a lower limit for
640 summer/fall emissions. The Padilla et al. (2019) survey was calibrated by an inverted seep flux buoy suspended at 23
641 m. This differs significantly from seep flux buoy measurements (Washburn et al., 2001), which are collected in surface
642 drift mode. Surface drift mode ensures a horizontal orientation for the buoy and an absence of lateral velocity
643 difference between the capture device and currents – either of which decreases capture efficiency from 100%, biasing
644 derived emissions low. Further, the Padilla et al. (2019) survey was calibrated 1 month after the sonar surveys, whereas
645 the 1995 engineered plume calibration by Hornafius et al. (1999) was contemporaneous. The Hornafius et al. (1999)
646 approach accounts (partially) for dissolution between the seabed and survey depth window, albeit air dissolves slower
647 than methane. Dissolution losses between the seabed and the depth window can be addressed by a numerical bubble
648 model (Leifer et al., 2017).

649

650 The Gaussian plume model-derived E_A was $8.4 \times 10^4 \text{ m}^3 \text{ dy}^{-1}$. Based on the Clark et al. (2000) assessment that half the
651 seabed seepage reaches the atmosphere, $E_B=1.7 \times 10^5 \text{ m}^3 \text{ dy}^{-1}$; very similar to $E_B=1.5 \times 10^5 \text{ m}^3 \text{ dy}^{-1}$ from Hornafius et al.
652 (1999). This agreement is coincidental as it neglects seasonal and interannual trends. For example, Bradley et al.
653 (2010) found 1994-1996 emissions were well below the average for 1990-2008, increasing significantly after 2008.

654

655 **4.2.2 Methane and non-methane hydrocarbon emissions**

656 Analysis of atmospheric samples provided a picture of the complexity of atmospheric emissions that arises from the
657 multiple pathways underlying atmospheric emissions. Specifically, as bubbles rise, they lose lighter and more soluble
658 gases faster (deeper in the water column), leading to differences between evasion from dissolved gases and direct
659 bubble transport (Leifer & Clark, 2002). Thus, bubble-mediated transport enhances larger alkanes relative to smaller

660 alkanes leaving more of the smaller alkanes in the water column. For strong seeps, bubble plumes are associated with
661 strong upwelling flows (Leifer et al., 2009), which transport dissolved gases to the sea surface where they outgas.
662 Additionally, oil (as droplets and bubble coatings) enhances alkane transport due to slower dissolution and diffusion
663 of larger alkanes through oil.

664
665 Atmospheric plume concentrations were 11.5% NMHC and 88.5% CH₄, very similar to Hornafius et al. (1999) who
666 referenced the Seep Tent composition (88% CH₄, 10% NMHC, and 2% nitrogen) as very similar to the reservoir
667 composition. Note, Clark et al. (2010) observed Trilogy near sea surface bubbles with 5.7% to 7.9% NMHC and 52.4
668 to 79.7% CH₄, demonstrating significant partitioning. The similarity between the atmospheric and seabed composition
669 despite the difference in the bubble composition demonstrates efficient dissolved gas transfer to the sea surface.

670
671 COP seep field seabed emissions are orders of magnitude greater than typically reported for other seep areas, e.g.,
672 summary Römer et al. (2017) where emissions for 12 different seep areas including sites in the North Sea, Pacific
673 northwest, Gulf of Mexico, etc., were 2-480 tons yr⁻¹, multiple orders of magnitude less than COP seep field seabed
674 emissions. Römer et al. (2017) used a bubble model for Dogger Bank seepage in the North Sea to estimate emissions
675 for observed atmospheric CH₄ plumes. The model estimated direct atmospheric bubble-mediated emissions of 21.7
676 ton yr⁻¹, 20% of seabed emissions. For the Tommelieten Seeps (in 70-m water) Schneider von Deimling et al. (2011)
677 estimated 4% of the 0.024 Gg CH₄ yr⁻¹ seabed emissions, i.e., ~1 Mg CH₄ yr⁻¹ reached the atmosphere by bubble-
678 mediated transfer. Schneider von Deimling et al. (2011) used a bubble model based on an assumed bubble size and
679 neglected diffusive flux. These diffusive fluxes include bubble dissolution into the wave mixed layer in the local area.
680 A few studies have directly measured atmospheric fluxes by an air-sea gas transfer model. For example, Schmale,
681 Beaubien, Rehder, Greinert, and Lonmbardi (2010) found seep air fluxes of 0.96-2.32 nmol m⁻² s⁻¹, much higher than
682 the ambient Black Sea flux of 0.32-0.77 nmol m⁻² s⁻¹. In the Black Sea, ambient emissions arise from microbially
683 produced CH₄ in shelf and slope sediments (Reeburgh et al., 1991). Di, Feng, and Chen (2019) estimated 7.7 nmol m⁻²
684 s⁻¹ for the shallow South China Sea based on an air-sea gas transfer model. If we disperse COP seep field atmospheric
685 emissions of 1.15x10⁹ M yr⁻¹ over the ~6.3 km² of 25x25 m² bins with emissions, we find 5.7 μM m⁻² s⁻¹, three orders
686 of magnitude greater.

687
688 Recent estimates of total global geo-CH₄ sources from a bottom-up approach are 45 Tg yr⁻¹ with submarine seepage
689 contributing 7 Tg yr⁻¹ (Etiope & Schwietzke, 2019), implying COP seep field contributes 0.25% of the bottom-up
690 submarine emissions. However, an estimate of pre-industrial CH₄ emissions (not confounded with fossil fuel
691 production emissions) based on ice core ¹⁴CH₄ suggested 1.6 Tg geo-CH₄ yr⁻¹ emissions (Hmiel et al., 2020). This
692 estimate, if accurate, would imply the COP seep field contributes an astounding 1% of global seep emissions
693 (submarine and aerial) and is difficult to reconcile with the COP seep field and other top seepage estimates. For
694 example, CH₄ atmospheric emissions for the Lusi hydrothermal system of 0.1 Tg yr⁻¹ (Mazzini et al., 2021), a hotspot
695 in the Laptev Sea of 0.9 Tg yr⁻¹ into shallow seas (Shakhova, Semiletov, Leifer, et al., 2010), and for the East Siberian

696 Arctic Sea using eddy covariance of 3.0 Tg yr^{-1} (Thornton et al., 2020). Thus, COP seep field emissions either play a
697 significant role in global seep emissions or indicate that geo-gas emissions are less tightly constrained.

698
699 COP seep field C_2H_6 emissions were $1.27 \text{ Gg C}_2\text{H}_6 \text{ yr}^{-1}$. For reference, this is 11% of the $11.4 \text{ Gg C}_2\text{H}_6 \text{ yr}^{-1}$ in 2010
700 for the South Coast Air Basin (SCAB), which includes Los Angeles (Peischl et al., 2013). Globally, Simpson et al.
701 (2012) and Höglund-Isaksson (2017) found 11.3 and $9.7 \text{ Tg C}_2\text{H}_6 \text{ yr}^{-1}$ in 2010, respectively. C_2H_6 has been increasing
702 since 2010 due to increased O&G production emissions (Helmig et al., 2016). Globally, seeps are estimated to
703 contribute $2\text{-}4 \text{ Tg C}_2\text{H}_6 \text{ yr}^{-1}$ (Etiopie & Ciccioli, 2009), and from ice cores, $2.2\text{-}3.5 \text{ Tg yr}^{-1}$ (Nicewonger, Verhulst,
704 Aydin, & Saltzman, 2016). This suggests the seep field contributes $0.03\text{-}0.06\%$ of global seep emissions.

705
706 Seep THC was 4.2% propane, implying emissions of $2.5 \text{ Gg C}_3\text{H}_8 \text{ yr}^{-1}$. Global propane emissions are 10.5 Tg yr^{-1}
707 (Poizzer et al., 2010), with $1\text{-}2 \text{ Tg yr}^{-1}$ estimated for seeps (Etiopie & Ciccioli, 2009). This suggests the COP seep field
708 contributes $0.05\text{-}0.1\%$ of the global seep budget. Oceans are estimated to contribute $0.35 \text{ Tg C}_3\text{H}_8 \text{ yr}^{-1}$ (Poizzer et al.,
709 2010), less than geological seepage contribution.

710
711 Based on an evaluation of the COP seep field emissions with respect to global seep ethane and propane emissions,
712 COP seep field contribution to global geo- CH_4 emissions are consistent with recent global geo-gas CH_4 emissions
713 estimates of 45 Tg yr^{-1} (0.04%) (Etiopie et al., 2019), not the significantly lower pre-industrial estimates of global geo-
714 CH_4 emissions, e.g., 1.6 Tg yr^{-1} (1.15%) (Hmiel et al., 2020).

715
716 Global butane emissions are $14 \text{ Tg C}_4\text{H}_{10} \text{ yr}^{-1}$ (Poizzer et al., 2010), higher than ethane and propane. COP seep field
717 butane (C_4) and pentane (C_5) emissions were $2.2 \text{ Gg C}_4\text{H}_{10} \text{ yr}^{-1}$ and $1.1 \text{ Gg C}_5\text{H}_{12} \text{ yr}^{-1}$, respectively, thus combined $\text{C}_2\text{-}$
718 C_5 emissions are 7.1 Gg yr^{-1} , compared to 65 Gg yr^{-1} from the entire SCAB, i.e., COP seep field contributes $\sim 5\%$ the
719 SCAB. COP $\text{C}_2\text{-C}_5$ emissions are significantly above that of the La Brea area, estimated at 1.7 Gg yr^{-1} (Weber et al.,
720 2017). Note, COP seep field atmospheric $\text{C}_2\text{-C}_5$ emissions certainly are larger, potentially significantly, as larger
721 alkanes also are emitted from oil slicks but were not considered for this study, and furthermore, the atmospheric plume
722 from the slicks was not sampled for this study.

723
724 Both benzene and toluene were detected with estimated emissions of 5000 and 1300 kg yr^{-1} , respectively. These
725 emissions likely are underestimates, potentially significantly, due to neglecting the oil slick evaporation contribution.
726 Both gases are of significant health concerns, as are alkanes like pentane and hexane.

727

728 **4.3 Downcurrent emissions**

729 The seep field concentration, $C'(\theta)$, anomaly was centered at $\theta \sim 200^\circ$ and well matched the location of the seep field,
730 and moreover, was well described by a dual Gaussian function (**Fig. 4B**). This was surprising given that the seep field
731 is asymmetric with respect to a 200° axial line from WCS to COP. Underlying this seeming discrepancy is that WCS

732 winds are weakest from due south and strongest from the west (prevailing) and also stronger to the east-southeast
733 (**Fig. 4C**).

734
735 The residual of the Gaussian fit increased in the downcurrent direction (**Supp. Fig. S9B**), consistent with evasion from
736 the downcurrent dissolved plume and seepage from this area. The dissolved plume roughly follows the coast,
737 extending as far as $\sim 280^\circ$ from WCS due to the coastline shift from northwest to west around Haskell Beach (**Fig. 2**),
738 $\sim 30^\circ$ beyond the seep field's sonar mapped western edge (**Fig. 1**). As prevailing winds are westerlies (paralleling the
739 coastal mountains), downcurrent plume evasions decrease with distance due to dispersion and also as surface waters
740 become depleted by evasion. Evasion increases non-linearly with u , particularly for winds that include wave breaking
741 (Nightingale et al., 2000); however, higher winds also dilute emissions. Note, there are no mapped seeps in this area.

742
743 Dissolved plume emissions also likely occur from east of the field, leading the model to emphasize seepage at the
744 field's eastern extent, too. Specifically, strong prevailing afternoon westerly surface winds drive a near-surface
745 dissolved plume eastwards. When these westerly winds calm down late in the evening, easterly winds transport
746 evasion from this east-displaced dissolved plume towards WCS. Additionally, it also is possible that the COP seep
747 field extends further east than mapped in sonar surveys, at least during some seasons.

748

749 **4.4 Focused seep area emissions**

750 Trilogy Seep area emissions were estimated at $6,200 \text{ m}^3 \text{ CH}_4 \text{ dy}^{-1}$ in May 2016. For comparison, Clark et al. (2010)
751 found 5500 and $4200 \text{ m}^3 \text{ THC dy}^{-1}$ ($4,900$ and $3,700 \text{ m}^3 \text{ CH}_4 \text{ dy}^{-1}$) for Trilogy Seep as measured by flux buoy for near
752 surface bubble fluxes in Sept. 2005. Note, the plume inversion approach also includes outgassing of near surface
753 waters that have enhanced C_{CH_4} from plume dissolution, which the flux buoy approach does not include. Although
754 Clark et al. (2010) found surface bubbles had undetectable CO_2 , the atmospheric plume's CO_2 to CH_4 concentration
755 ratio was comparable to the seabed bubble concentration ratio. This demonstrates significant upwelling flow transport
756 of seabed water to the sea surface where dissolved gases evade near where the bubble plume surfaces. This near-plume
757 evasion contributes to the atmospheric plume. Note, these emissions neglect downcurrent emissions. A 50:50
758 atmosphere:ocean partitioning suggests 2016 Trilogy Seep emissions were $\sim 40\%$ lower than in 2005 – a difference
759 within the difference between the two 2005 Trilogy Seep measurements Clark et al. (2010).

760
761 In contrast, agreement was very poor for the Seep Tent Seep, for which Clark et al. (2010) mapped emissions of 5700
762 $\text{m}^3 \text{ day}^{-1}$ ($5000 \text{ m}^3 \text{ CH}_4 \text{ day}^{-1}$) in Nov. 2002 whereas this study found $310 \text{ m}^3 \text{ CH}_4 \text{ dy}^{-1}$. This discrepancy was readily
763 apparent with almost no visible surface bubble expression in May 2016, whereas the Seep Tent Seep has been a
764 perennial feature since its appearance. The absence of more than a few scattered bubbles at the sea surface (the boil
765 in 2000 was driven by a $1\text{-}2 \text{ m s}^{-1}$ upwelling - Leifer, Clark, and Chen (2000) - indicates that most emissions are from
766 evasion. A buoyancy plume associated with the rising oil (thick oil slicks surface above the Seep Tents) as well as
767 methane dissolved in the oil likely are transporting the observed, focused CH_4 emissions.

768
769 This is remarkable given that the seep field's geofluid migration "center" in recent decades has been the Seep Tent
770 Seep (Bradley et al., 2010), which was the largest seep in the field in 2010 (Clark et al., 2010). The Seep Tent Seep
771 consists of emissions not captured by the Seep Tents – two large (33-m square) steel capture tents on the seafloor. For
772 reference, the Seep Tents captured $\sim 16,800 \text{ m}^3 \text{ gas dy}^{-1}$ in the early 2000s (Boles et al., 2001). Bradley et al. (2010)
773 found in WCS data that when overall seep field emissions decreased to a minimum in 1995, they were focused on the
774 Seep Tent Seep direction. Note, the Seep Tent Seep was observed first in 1970 as a boil visible from 1.6-km distant.
775 The seepage was tented in Sept. 1982 (Boles et al., 2001).

776
777 Underlying these observations are several factors. First, the Seep Tent Seep is modern – since 1978 – as it was not
778 mapped in a 1953 seep survey (Leifer, 2019). At the time it was first reported as a sea boil visible over a kilometer
779 distant (Boles et al., 2001). Since installation, overall Seep Tent production has diminished (Boles et al., 2001) by a
780 factor of 3 from 1984 to 1995. Some fraction of this trend could have resulted from the expansion of active seepage
781 beyond the seep tents. Perhaps more significantly, the Seep Tent Seep lies over one of the Platform Holly wells (Leifer
782 et al., 2010; Fig. 3C), creating the potential of linkage between well production (including stimulation) and Seep Tent
783 production and thus Seep Tent seepage (the uncaptured portion).

784

785 **4.6 Diurnal trend and bias**

786 The diurnal wind patterns typical of the coastal Pacific marine environment are weak offshore (northerly) night winds
787 that shift to from the east in the morning and then swing to from the south. In afternoon they strengthen and shift to
788 prevailing westerlies, continuing to late in the evening (Bradley et al., 2010). Note, WCS seep emissions require winds
789 to "probe or scan" across the seep field, and thus miss the strong afternoon prevailing winds when emissions are
790 expected to be higher. This is because higher wind speeds increase sea-air gas emissions of dissolved near-surface
791 gases (Nightingale et al., 2000) and increase emissions from higher hydrostatic pressure fluctuation driven by wave
792 height (Leifer & Boles, 2005). Given that prevailing winds are westerlies, higher afternoon emissions will generally
793 (but not always) drift eastwards, missing WCS.

794

795 The diurnal wind pattern from the seep field direction is different from the overall (direction-independent) diurnal
796 pattern. Typical nocturnal winds are quite weak, $1.5\text{--}1.7 \text{ m s}^{-1}$ (Fig. 6). The strongest diurnal wind change was from
797 late night to morning, a 20% decrease. Onshore winds (seep direction) in the middle of the night are from synoptic
798 systems and were associated with the highest C' . Winds increase by a few percent to an early afternoon peak,
799 decreasing through early evening before increasing again later in the night.

800

801 The diurnal trend for C from the seep direction followed the diurnal wind cycle, increasing by ~ 20 ppb and peaking
802 ~ 2 hours later in the day than winds (15:00 versus 13:00 for C compared to u , respectively). This may reflect the lag

803 in wave development with respect to wind strengthening and transport time. Based on sensitivity studies, the diurnal
804 cycles in u and C correspond to variations of $\sim 7\%$ and $\sim 9\%$ in E_A .

805
806 Although efforts were made to characterize the diurnal cycle from WCS data, WCS data poorly sample the seep field
807 for the higher wind speeds that occur in the afternoon which primarily are westerlies. Note, non-linearity in sea-air
808 evasion with u means the model use of average u underestimates E_A . Thus, the contribution of the prevailing afternoon
809 winds to diurnal emissions is significantly underestimated from WCS data. It is worth noting, though, that this factor
810 only affects 25-33% of diurnal emissions. As the true diurnal cycle cannot be derived from WCS data, field data of
811 repeat transects spanning the different phases of a diurnal cycle are needed.

812

813 **4.7 Future needs and improvements**

814 The sensitivity studies identified areas for improvement and data gaps. These are described in brief below and in more
815 detail in **Supp. Sec. S8**. The largest uncertainty was with regards to partitioning between the inshore and offshore seep
816 trends, which could be determined by a second air quality station, preferably including speciation such as by CEAS
817 analyzers of CH_4 and C_2H_6 . Further simulations could add grid cells for evasion corresponding to the downcurrent
818 plumes to assess their contribution. The model was limited by available workstation power; however, additional
819 computation power could open improvements such as simulating a range of wind speed based on the wind speed
820 probability distribution with respect to wind direction, $\phi(u, \theta)$.

821
822 Additional field work and data also are needed. Another important sensitivity was to boundary layer height, BL , which
823 varies diurnally and seasonally (Dorman & Winant, 2000) and could be derived from ceilometer data (Münkel, 2007).
824 Another significant concern is afternoon seep field emissions that bypass WCS, which could be addressed by field
825 work and a second air quality station at a different downwind direction from the seep field. Mapping offshore wind
826 fields to characterize wind veering across the seep field is needed to allow simulations to provide insights at the seep
827 area size-scale.

828

829 **5 Conclusions**

830 In this study, data from an onshore air quality station located downwind of a large marine seep field was analysed to
831 derive the three-decade-averaged seep field emissions using an inversion model. The modeled emissions were similar
832 to reported emissions; however, this was coincidental given that prior reported emissions were during a period of field
833 quiescence. Highlighting the significance of the COP seep field, ethane and propane emissions suggest the COP seep
834 field contributes 0.04% and 0.12% of the global seep budget, respectively. As a result, COP seep field emissions of
835 $19 \text{ Tg CH}_4 \text{ yr}^{-1}$ are consistent with global geo-gas budgets of 45 Tg yr^{-1} , but inconsistent with significantly lower
836 emissions estimated from ice core isotopic data. Additionally, the approach could be adapted to air quality station data

837 for other sources including terrestrial seeps, production fields, etc., if the sources are spatially constrained and isolated
838 from confounding sources.

839

840 **Data availability.** All data needed to evaluate the conclusions in the paper are present in the paper and/or the
841 Supplementary Materials and/or were submitted to the Mendeley Data Repository, see Leifer, Ira (2020),
842 “Seep_Air_Data”, Mendeley Data, V1, <http://dx.doi.org/10.17632/znhxkftm8.1>
843

844 **Supplement.** The supplement contains additional supporting figures and details to complement the manuscript and
845 an interactive map file as a Google Earth archive of the offshore survey data that are presented in **Fig. 2**.

846

847 **Author Contributions.** IL Developed and conducted the study, analysed data, and wrote the manuscript. CM analysed
848 data and edited the manuscript. DB analysed air sample data and edited the manuscript.

849

850 **Competing interests.** The authors declare that they have no conflict of interest.

851

852 **Acknowledgements.** We would like to gratefully acknowledge the SBCAPCD for providing data from their ongoing
853 monitoring program and the contribution of Marc Moritsch and Joel S. Cordes in particular for help with these data,
854 and Doug Wilson for the processed sonar data. We recognize the skill and participation of vessel captains Jeff Wright
855 and Tony Vultaggio and editorial review by Charlotte Marston, Bubbleology Research International.

856

857 **Financial Support.** This work was supported by Plains All American Pipeline and the Bubbleology Research
858 International, Internal Research and Development (IRAD) fund.

859

860 **References**

- 861 Abrams, M. A. (2005). Significance of hydrocarbon seepage relative to petroleum generation and
 862 entrapment. *Marine and Petroleum Geology*, 22(4), 457-477.
 863 doi:10.1016/j.marpetgeo.2004.08.003
- 864 Abrams, M. A. (2017). Evaluation of near-surface gases in marine sediments to assess
 865 subsurface petroleum gas generation and entrapment. *Geosciences*, 7(2), 35.
 866 doi:10.3390/geosciences7020035
- 867 Bernard, B. B., Brooks, J. M., & Zumberge, J. (2001, 16-19 September 2001). *Determining the*
 868 *origin of gases in near-surface sediments*. Paper presented at the AAPG Hedberg
 869 Conference, Vancouver BC, Canada.
- 870 Boles, J. R., Clark, J. F., Leifer, I., & Washburn, L. (2001). Temporal variation in natural
 871 methane seep rate due to tides, Coal Oil Point area, California. *Journal Geophysical*
 872 *Research - Oceans*, 106(C11), 27,077-027,086. doi:10.1029/2000JC000774
- 873 Borges, A. V., Champenois, W., Gypens, N., Delille, B., & Harlay, J. (2016). Massive marine
 874 methane emissions from near-shore shallow coastal areas. *Scientific Reports*, 6, 27908.
 875 doi:10.1038/srep27908
- 876 Bradley, E. S., Leifer, I., & Roberts, D. A. (2010). Long-term monitoring of a marine geologic
 877 hydrocarbon source by a coastal air pollution station in Southern California. *Atmospheric*
 878 *Environment*, 44(38), 4973-4981. doi:10.1016/j.atmosenv.2010.08.010
- 879 CDOGGR. (2018). Well Finder. Retrieved from
 880 <https://www.conservation.ca.gov/dog/Pages/Wellfinder.aspx>. Retrieved 6 May 2019,
 881 from California Department of Conservation
 882 <https://www.conservation.ca.gov/dog/Pages/Wellfinder.aspx>
- 883 Clark, J. F., Washburn, L., Hornafius, J. S., & Luyendyk, B. P. (2000). Natural marine
 884 hydrocarbon seep source of dissolved methane to California coastal waters. *Journal*
 885 *Geophysical Research - Oceans*, 105, 11,509-511,522. doi:10.1029/2000JC000259
- 886 Clark, J. F., Washburn, L., & Schwager, K. (2010). Variability of gas composition and flux
 887 intensity in natural marine hydrocarbon seeps. *Geo-Marine Letters*, 30, 379-388.
 888 doi:10.1007/s00367-009-0167-1
- 889 Di, P., Feng, D., & Chen, D. (2019). The distribution of dissolved methane and its air-sea flux in
 890 the plume of a seep field, Lingtou Promontory, South China Sea. *Geofluids*, 2019,
 891 3240697. doi:10.1155/2019/3240697
- 892 Di, P., Feng, D., Tao, J., & Chen, D. (2020). Using time-series videos to quantify methane
 893 bubbles flux from natural cold seeps in the South China Sea. *Minerals*, 10(3), 216.
 894 doi:10.3390/min10030216
- 895 Dorman, C. E., & Winant, C. D. (2000). The structure and variability of the marine atmosphere
 896 around the Santa Barbara Channel. *Monthly Weather Review*, 128(2), 261-282.
 897 doi:10.1175/1520-0493(2000)128<0261
- 898 Edinger, J. G. (1959). Changes in the depth of the marine layer over the Los Angeles Basin.
 899 *Journal of Meteorology*, 16(3), 219-226. doi:10.1175/1520-
 900 0469(1959)016<0219:citdot>2.0.co;2
- 901 Etiope, G., & Cicciooli, P. (2009). Earth's degassing: A missing ethane and propane source.
 902 *Science*, 323(5913), 478-478. doi:10.1126/science.1165904
- 903 Etiope, G., Ciotoli, G., Schwietzke, S., & Schoell, M. (2019). Gridded maps of geological
 904 methane emissions and their isotopic signature. *Earth System Science Data*, 11(1), 1-22.
 905 doi:10.5194/essd-11-1-2019

906 Etiope, G., & Schwietzke, S. (2019). Global geological methane emissions: An update of top-
907 down and bottom-up estimates. *Elementa: Science of the Anthropocene*, 7.
908 doi:10.1525/elementa.383

909 Fischer, P. J. (1978). Oil and Tar Seeps, Santa Barbara Basin, California. In D. J. Everitts, R. G.
910 Paul, C. F. Eaton, & E. E. Welay (Eds.), *California Offshore Gas, Oil and Tar Seeps*
911 (pp. 1-62). Sacramento, California: California State Lands Commission.

912 Freeworldmaps (Cartographer). (2020). Physical Map of California. Retrieved from
913 <https://www.freeworldmaps.net/united-states/california/map.html>

914 Frew, N. M., Bock, E. J., Schimpf, U., Hara, T., Haußecker, H., Edson, J. B., . . . Jähne, B.
915 (2004). Air-sea gas transfer: Its dependence on wind stress, small-scale roughness, and
916 surface films. *Journal of Geophysical Research: Oceans*, 109(C8), C08S17.
917 doi:10.1029/2003JC002131

918 Greinert, J. (2008). Monitoring temporal variability of bubble release at seeps: The
919 hydroacoustic swath system GasQuant. *Journal of Geophysical Research*, 113, C07048.
920 doi:10.1029/2007JC004704

921 Greinert, J., McGinnis, D. F., Naudts, L., Linke, P., & De Batist, M. (2010). Atmospheric
922 methane flux from bubbling seeps: Spatially extrapolated quantification from a Black Sea
923 shelf area. *Journal of Geophysical Research*, 115. doi:10.1029/2009jc005381

924 Hanna, S. R., Briggs, G. A., & Hosker Jr., R. P. (1982). *Handbook on Atmospheric Diffusion* (J.
925 S. Smith Ed.): Technical Information Center, U.S. Department of Energy.

926 Helmig, D., Rossabi, S., Hueber, J., Tans, P., Montzka, S. A., Masarie, K., . . . Pozzer, A. (2016).
927 Reversal of global atmospheric ethane and propane trends largely due to US oil and
928 natural gas production. *Nature Geoscience*, 9(7), 490-495. doi:10.1038/ngeo2721

929 Heyer, J., & Berger, U. (2000). Methane emission from the coastal area in the Southern Baltic
930 Sea. *Estuarine, Coastal and Shelf Science*, 51(1), 13-30. doi:10.1006/ecs.2000.0616

931 Higgs, B., Mountjoy, J. J., Crutchley, G. J., Townend, J., Ladroit, Y., Greinert, J., & McGovern,
932 C. (2019). Seep-bubble characteristics and gas flow rates from a shallow-water, high-
933 density seep field on the shelf-to-slope transition of the Hikurangi subduction margin.
934 *Marine Geology*, 417, 105985. doi:10.1016/j.margeo.2019.105985

935 Hmiel, B., Petrenko, V. V., Dyonisius, M. N., Buizert, C., Smith, A. M., Place, P. F., . . .
936 Dlugokencky, E. (2020). Preindustrial 14CH₄ indicates greater anthropogenic fossil CH₄
937 emissions. *Nature*, 578(7795), 409-412. doi:10.1038/s41586-020-1991-8

938 Höglund-Isaksson, L. (2017). Bottom-up simulations of methane and ethane emissions from
939 global oil and gas systems 1980 to 2012. *Environmental Research Letters*, 12(2), 024007.
940 doi:10.1088/1748-9326/aa583e

941 Hornafius, S. J., Quigley, D. C., & Luyendyk, B. P. (1999). The world's most spectacular marine
942 hydrocarbons seeps (Coal Oil Point, Santa Barbara Channel, California): Quantification
943 of emissions. *Journal Geophysical Research - Oceans*, 104(C9), 20,703-720,711.
944 doi:10.1029/1999JC900148

945 Hughes, M., Hall, A., & Fovell, R. G. (2007). Dynamical controls on the diurnal cycle of
946 temperature in complex topography. *Climate Dynamics*, 29(2), 277-292.
947 doi:10.1007/s00382-007-0239-8

948 IEA. (2020). *Methane Tracker 2020*. Retrieved from Paris: [https://www.iea.org/reports/methane-](https://www.iea.org/reports/methane-tracker-2020)
949 [tracker-2020](https://www.iea.org/reports/methane-tracker-2020)

- 950 IPCC. (2013). *Working Group I Contribution to the IPCC Fifth Assessment Report Climate*
951 *Change 2013-The Physical Science Basis*. Retrieved from IPCC Secretariat, Geneva,
952 Switzerland:
- 953 IPCC. (2014). *Climate Change 2014: Synthesis Report. Contributions of Working Groups I, II*
954 *and III to the Fifth Assessment Report of the Intergovernmental Panel on Climate*
955 *Change*. Retrieved from Geneva, Switzerland: [http://www.ipcc.ch/pdf/assessment-](http://www.ipcc.ch/pdf/assessment-report/ar5/syr/SYR_AR5_FINAL_full_wcover.pdf)
956 [report/ar5/syr/SYR_AR5_FINAL_full_wcover.pdf](http://www.ipcc.ch/pdf/assessment-report/ar5/syr/SYR_AR5_FINAL_full_wcover.pdf)
- 957 Jackson, R. B., Saunois, M., Bousquet, P., Canadell, J. G., Poulter, B., Stavert, A. R., . . .
958 Tsuruta, A. (2020). Increasing anthropogenic methane emissions arise equally from
959 agricultural and fossil fuel sources. *Environmental Research Letters*, *15*(7), 071002.
960 doi:10.1088/1748-9326/ab9ed2
- 961 Johansen, C., Macelloni, L., Natter, M., Silva, M., Woosley, M., Woolsey, A., . . . MacDonald, I.
962 R. (2020). Hydrocarbon migration pathway and methane budget for a Gulf of Mexico
963 natural seep site: Green Canyon 600. *Earth and Planetary Science Letters*, *545*, 116411.
964 doi:10.1016/j.epsl.2020.116411
- 965 Jordan, S. F. A., Treude, T., Leifer, I., Janßen, R., Werner, J., Schulz-Vogt, H., & Schmale, O.
966 (2020). Bubble-mediated transport of benthic microorganisms into the water column:
967 Identification of methanotrophs and implication of seepage intensity on transport
968 efficiency. *Scientific Reports*, *10*(1), 4682. doi:10.1038/s41598-020-61446-9
- 969 Judd, A., & Hovland, M. (2007). *Seabed fluid flow: The impact on geology, biology and the*
970 *marine environment*. Cambridge, UK: Cambridge University Press.
- 971 Kasaya, T., Mitsuzawa, K., Goto, T.-n., Iwase, R., Sayanagi, K., Araki, E., . . . Nagao, T. (2009).
972 Trial of multidisciplinary observation at an expandable sub-marine cabled station “Off-
973 Hatsushima Island Observatory” in Sagami Bay, Japan. *Sensors*, *9*(11), 9241-9254.
974 doi:10.3390/s91109241
- 975 Leifer, I. (2010). Characteristics and scaling of bubble plumes from marine hydrocarbon seepage
976 in the Coal Oil Point seep field. *Journal Geophysical Research*, *115*(C11), C11014.
977 doi:10.1029/2009JC005844
- 978 Leifer, I. (2015). Seabed bubble flux estimation by calibrated video survey for a large blowout
979 seep in the North Sea. *Journal of Marine and Petroleum Geology*, *68B*, 743-752.
980 doi:10.1016/j.marpetgeo.2015.08.032
- 981 Leifer, I. (2019). A synthesis review of emissions and fates for the Coal Oil Point marine
982 hydrocarbon seep field and California marine seepage. *Geofluids*, *2019*(4724587), 1-48.
983 doi:10.1155/2019/4724587
- 984 Leifer, I., & Boles, J. (2005). Turbine tent measurements of marine hydrocarbon seeps on
985 subhourly timescales. *Journal of Geophysical Research-Oceans*, *110*(C1), C01006.
986 doi:10.1029/2003jc002207
- 987 Leifer, I., Boles, J. R., Luyendyk, B. P., & Clark, J. F. (2004). Transient discharges from marine
988 hydrocarbon seeps: Spatial and temporal variability. *Environmental Geology*, *46*(8),
989 1038-1052. doi:10.1007/s00254-004-1091-3
- 990 Leifer, I., Chernykh, D., Shakhova, N., & Semiletov, I. (2017). Sonar gas flux estimation by
991 bubble insonification: Application to methane bubble flux from seep areas in the outer
992 Laptev Sea. *The Cryosphere*, *11*(3), 1333-1350. doi:10.5194/tc-11-1333-2017
- 993 Leifer, I., & Clark, J. F. (2002). Modeling trace gases in hydrocarbon seep bubbles: Application
994 to marine hydrocarbon seeps in the Santa Barbara Channel. *Geologiya I Geofizika*, *47*(7),
995 572-579.

- 996 Leifer, I., Clark, J. F., & Chen, R. F. (2000). Modifications of the local environment by natural
 997 marine hydrocarbon seeps. *Geophysical Research Letters*, 27(22), 3711-3714.
 998 doi:10.1029/2000GL011619
- 999 Leifer, I., Jeuthé, H., Gjøssund, S. H., & Johansen, V. (2009). Engineered and natural marine
 1000 seep, bubble-driven buoyancy flows. *Journal of Physical Oceanography*, 39(12), 3071-
 1001 3090. doi:10.1175/2009JPO4135.1
- 1002 Leifer, I., Kamerling, M., Luyendyk, B. P., & Wilson, D. (2010). Geologic control of natural
 1003 marine hydrocarbon seep emissions, Coal Oil Point seep field, California. *Geo-Marine
 1004 Letters*, 30(3-4), 331-338. doi:10.1007/s00367-010-0188-9
- 1005 Leifer, I., Luyendyk, B. P., Boles, J., & Clark, J. F. (2006). Natural marine seepage blowout:
 1006 Contribution to atmospheric methane. *Global Biogeochemical Cycles*, 20(3), GB3008.
 1007 doi:10.1029/2005GB002668
- 1008 Leifer, I., & MacDonald, I. (2003). Dynamics of the gas flux from shallow gas hydrate deposits:
 1009 interaction between oily hydrate bubbles and the oceanic environment. *Earth and
 1010 Planetary Science Letters*, 210(3-4), 411-424. doi:10.1016/S0012-821X(03)00173-0
- 1011 Leifer, I., Melton, C., Fischer, M. L., Fladeland, M., Frash, J., Gore, W., . . . Yates, E. L. (2018).
 1012 Atmospheric characterization through fused mobile airborne and surface in situ surveys:
 1013 Methane emissions quantification from a producing oil field. *Atmospheric Measurement
 1014 Techniques*, 11(3), 1689-1705. doi:10.5194/amt-11-1689-2018
- 1015 Leifer, I., Melton, C., Manish, G., & Leen, B. (2014). Mobile monitoring of methane leakage.
 1016 *Gases and Instrumentation*, July/August 2014, 20-24.
- 1017 Leifer, I., Melton, C., Tratt, D. M., Buckland, K. N., Chang, C., Frash, J., . . . Yurganov, L.
 1018 (2018). Validation of mobile in situ measurements of dairy husbandry emissions by
 1019 fusion of airborne/surface remote sensing with seasonal context from the Chino Dairy
 1020 Complex. *Environmental Pollution*, 242(Pt B), 2111-2134.
 1021 doi:10.1016/j.envpol.2018.03.078
- 1022 Leifer, I., Melton, C., Tratt, D. M., Buckland, K. N., Clarisse, L., Coheur, P., . . . Yurganov, L.
 1023 (2016). Remote sensing and in situ measurements of methane and ammonia emissions
 1024 from a megacity dairy complex: Chino, CA. *Environmental Pollution*, 221, 37-51.
 1025 doi:10.1016/j.envpol.2016.09.083
- 1026 Leifer, I., & Patro, R. (2002). The bubble mechanism for methane transport from the shallow
 1027 seabed to the surface: A review and sensitivity study. *Continental Shelf Research*, 22(16),
 1028 2409-2428. doi:10.1016/S0278-4343(02)00065-1
- 1029 Leifer, I., Solomon, E., Schneider v. Deimling, J., Coffin, R., Rehder, G., & Linke, P. (2015).
 1030 The fate of bubbles in a large, intense bubble plume for stratified and unstratified water:
 1031 Numerical simulations of 22/4b expedition field data. *Journal of Marine and Petroleum
 1032 Geology*, 68B, 806-823. doi:10.1016/j.marpetgeo.2015.07.025
- 1033 Liss, P. S., & Duce, R. A. (2005). *The sea surface and global change*: Cambridge University
 1034 Press.
- 1035 Liss, P. S., & Merlivat, L. (1986). Air-sea gas exchange rates: Introduction and synthesis. In P.
 1036 Buat-Ménard (Ed.), *The Role of Air-Sea Exchange in Geochemical Cycling* (Vol. 185).
 1037 Dordrecht: Springer.
- 1038 Lu, R., Turco, R. P., & Jacobson, M. Z. (1997). An integrated air pollution modeling system for
 1039 urban and regional scales: 1. Structure and performance. *Journal of Geophysical
 1040 Research: Atmospheres*, 102(D5), 6063-6079. doi:10.1029/96jd03501

1041 Marinaro, G., Etiope, G., Bue, N. L., Favali, P., Papatheodorou, G., Christodoulou, D., . . . Rolin,
1042 J.-F. (2006). Monitoring of a methane-seeping pockmark by cabled benthic observatory
1043 (Patras Gulf, Greece). *Geo-Marine Letters*, 26(5), 297-302. doi:10.1007/s00367-006-
1044 0040-4

1045 Mazzini, A., Sciarra, A., Etiope, G., Sadavarte, P., Houweling, S., Pandey, S., & Husein, A.
1046 (2021). Relevant methane emission to the atmosphere from a geological gas
1047 manifestation. *Scientific Reports*, 11(1), 4138. doi:10.1038/s41598-021-83369-9

1048 Minor, S. A., Kellogg, K. S., Stanley, R. G., Gurrola, L. D., Keller, E. A., & Brandt, T. R.
1049 (Cartographer). (2009). Geologic Map of the Santa Barbara Coastal Plain Area, Santa
1050 Barbara County, California. Retrieved from <https://pubs.usgs.gov/sim/3001/>

1051 Münkkel, C. (2007). Mixing height determination with lidar ceilometers - Results from Helsinki
1052 Testbed. *Meteorologische Zeitschrift*, 16, 451-459. doi:10.1127/0941-2948/2007/0221

1053 Muyakshin, S. I., & Sauter, E. (2010). The hydroacoustic method for the quantification of the gas
1054 flux from a submersed bubble plume. *Oceanology*, 50(6), 995-1001.
1055 doi:10.1134/S0001437010060202

1056 Nicewonger, M. R., Verhulst, K. R., Aydin, M., & Saltzman, E. S. (2016). Preindustrial
1057 atmospheric ethane levels inferred from polar ice cores: A constraint on the geologic
1058 sources of atmospheric ethane and methane. *Geophysical Research Letters*, 43(1), 214-
1059 221. doi:<https://doi.org/10.1002/2015GL066854>

1060 Nightingale, P. D., Malin, G., Law, C. S., Watson, A. J., Liss, P. S., Liddicoat, M. I., . . . Upstill-
1061 Goddard, R. C. (2000). In situ evaluation of air-sea gas exchange parameterizations using
1062 novel conservative and volatile tracers. *Global Biogeochemical Cycles*, 14(1), 373-387.
1063 doi:10.1029/1999GB900091

1064 Nisbet, E. G., Manning, M. R., Dlugokencky, E. J., Fisher, R. E., Lowry, D., Michel, S. E., . . .
1065 White, J. W. C. (2019). Very strong atmospheric methane growth in the 4 years 2014–
1066 2017: Implications for the Paris Agreement. *Global Biogeochemical Cycles*, 33(3), 318-
1067 342. doi:10.1029/2018GB006009

1068 Olson, D. J. (1983). *Surface and subsurface geology of the Santa Barbara Goleta Metropolitan*
1069 *area, Santa Barbara County, California*. (MS). Oregon State University, Retrieved from
1070 [https://ir.library.oregonstate.edu/concern/graduate_thesis_or_dissertations/v692tb957?loc](https://ir.library.oregonstate.edu/concern/graduate_thesis_or_dissertations/v692tb957?locale=it)
1071 [ale=it](https://ir.library.oregonstate.edu/concern/graduate_thesis_or_dissertations/v692tb957?locale=it)

1072 Padilla, A. M., Loranger, S., Kinnaman, F. S., Valentine, D. L., & Weber, T. C. (2019). Modern
1073 assessment of natural hydrocarbon gas flux at the Coal Oil Point seep field, Santa
1074 Barbara, California. *Journal of Geophysical Research: Oceans*, 124(4), 2472-2484.
1075 doi:10.1029/2018jc014573

1076 Peischl, J., Ryerson, T. B., Brioude, J., Aikin, K. C., Andrews, A. E., Atlas, E., . . . Parrish, D. D.
1077 (2013). Quantifying sources of methane using light alkanes in the Los Angeles basin,
1078 California. *Journal of Geophysical Research: Atmospheres*, 118(10), 4974-4990.
1079 doi:10.1002/jgrd.50413

1080 Pozzer, A., Pollmann, J., Taraborrelli, D., Jöckel, P., Helmig, D., Tans, P., . . . Lelieveld, J.
1081 (2010). Observed and simulated global distribution and budget of atmospheric
1082 C₂-C₅ alkanes. *Atmospheric Chemistry and Physics*, 10(9),
1083 4403-4422. doi:10.5194/acp-10-4403-2010

1084 Rahn, D. A., Parish, T. R., & Leon, D. (2017). Synthesis of observations from the Precision
1085 Atmospheric Marine Boundary Layer Experiment (PreAMBLE). *Monthly Weather*
1086 *Review*, 145(6), 2325-2342. doi:10.1175/mwr-d-16-0373.1

1087 Reeburgh, W. S. (2007). Oceanic methane biogeochemistry. *Chemical Reviews*, 107(2), 486-513.
1088 doi:10.1021/cr050362v

1089 Reeburgh, W. S., Ward, B. B., Whalen, S. C., Sandbeck, K. A., Kilpatrick, K. A., & Kerkhof, L.
1090 J. (1991). Black Sea methane geochemistry. *Deep Sea Research Part A. Oceanographic*
1091 *Research Papers*, 38, S1189-S1210. doi:[https://doi.org/10.1016/S0198-0149\(10\)80030-5](https://doi.org/10.1016/S0198-0149(10)80030-5)

1092 Rehder, G., Keir, R. S., Suess, E., & Rhein, M. (1999). Methane in the Northern Atlantic
1093 controlled by microbial oxidation and atmospheric history. *Geophysical Research*
1094 *Letters*, 26(5), 587-590. doi:10.1029/1999GL900049

1095 Riedel, M., Scherwath, M., Römer, M., Veloso, M., Heesemann, M., & Spence, G. D. (2018).
1096 Distributed natural gas venting offshore along the Cascadia margin. *Nature*
1097 *Communications*, 9(1), 3264. doi:10.1038/s41467-018-05736-x

1098 Römer, M., Hsu, C.-W., Loher, M., MacDonald, I. R., dos Santos Ferreira, C., Pape, T., . . .
1099 Sahling, H. (2019). Amount and fate of gas and oil discharged at 3400 m water depth
1100 from a natural seep site in the Southern Gulf of Mexico. *Frontiers in Marine Science*,
1101 6(700). doi:10.3389/fmars.2019.00700

1102 Römer, M., Riedel, M., Scherwath, M., Heesemann, M., & Spence, G. D. (2016). Tidally
1103 controlled gas bubble emissions: A comprehensive study using long-term monitoring data
1104 from the NEPTUNE cabled observatory offshore Vancouver Island. *Geochemistry,*
1105 *Geophysics, Geosystems*, 17(9), 3797-3814. doi:10.1002/2016GC006528

1106 Römer, M., Sahling, H., Pape, T., Bohrmann, G., & Spieß, V. (2012). Quantification of gas
1107 bubble emissions from submarine hydrocarbon seeps at the Makran continental margin
1108 (offshore Pakistan). *Journal of Geophysical Research: Oceans*, 117(C10), C10015.
1109 doi:10.1029/2011jc007424

1110 Römer, M., Wenau, S., Mau, S., Veloso, M., Greinert, J., Schlüter, M., & Bohrmann, G. (2017).
1111 Assessing marine gas emission activity and contribution to the atmospheric methane
1112 inventory: A multidisciplinary approach from the Dutch Dogger Bank seep area (North
1113 Sea). *Geochemistry, Geophysics, Geosystems*, 18(7), 2617-2633.
1114 doi:10.1002/2017gc006995

1115 Saunio, M., Stavert, A. R., Poulter, B., Bousquet, P., Canadell, J. G., Jackson, R. B., . . .
1116 Zhuang, Q. (2020). The global methane budget 2000-2017. *Earth System Science Data*,
1117 12(3), 1561-1623. doi:10.5194/essd-2019-128

1118 Sauter, E. J., Muyakshin, S. I., Charlou, J.-L., Schlüter, M., Boetius, A., Jerosch, K., . . . Klages,
1119 M. (2006). Methane discharge from a deep-sea submarine mud volcano into the upper
1120 water column by gas hydrate-coated methane bubbles. *Earth and Planetary Science*
1121 *Letters*, 243(3-4), 354-365. doi:10.1016/j.epsl.2006.01.041

1122 Scherwath, M., Thomsen, L., Riedel, M., Römer, M., Chatzievangelou, D., Schwendner, J., . . .
1123 Heesemann, M. (2019). Ocean observatories as a tool to advance gas hydrate research.
1124 *Earth and Space Science*, 6(12), 2644-2652. doi:10.1029/2019ea000762

1125 Schmale, O., Beaubien, S. E., Rehder, G., Greinert, J., & Lonmbardi, S. (2010). Gas seepage in
1126 the Dnepr paleo-delta area (NW-Black Sea) and its regional impact on the water column
1127 methane cycle. *Journal of Marine Systems*, 80(1-2), 90-100.
1128 doi:10.1016/j.jmarsys.2009.10.003

1129 Schmale, O., Greinert, J., & Rehder, G. (2005). Methane emission from high-intensity marine
1130 gas seeps in the Black Sea into the atmosphere. *Geophysical Research Letters*, 32(7),
1131 L07609. doi:10.1029/2004gl021138

1132 Schmale, O., Leifer, I., Stolle, C., Schneider von Deimling, J., Krause, S., Kießlich, K., . . .
1133 Treude, T. (2015). Bubble transport mechanism: Indications for a gas bubble-mediated
1134 inoculation of benthic methanotrophs into the water column. *Continental Shelf*
1135 *Research*, 103, 70-78. doi:10.1016/j.csr.2015.04.022

1136 Schneider von Deimling, J., Rehder, G., Greinert, J., McGinnis, D. F., Boetius, A., & Linke, P.
1137 (2011). Quantification of seep-related methane gas emissions at Tommeliten, North Sea.
1138 *Continental Shelf Research*, 31, 867-878. doi:10.1016/j.csr.2011.02.012

1139 Schwietzke, S., Sherwood, O. A., Bruhwiler, L. M. P., Miller, J. B., Etiope, G., Dlugokencky, E.
1140 J., . . . Tans, P. P. (2016). Upward revision of global fossil fuel methane emissions based
1141 on isotope database. *Nature*, 538(7623), 88-91. doi:10.1038/nature19797

1142 Shakhova, N., Semiletov, I., Leifer, I., Rekant, P., Salyuk, A., & Kosmach, D. (2010).
1143 Geochemical and geophysical evidence of methane release over the East Siberian Arctic
1144 Shelf. *Journal of Geophysical Research*, 115(C8), C08007. doi:10.1029/2009JC005602

1145 Shakhova, N., Semiletov, I., Salyuk, A., Iossoupov, V., Kosmach, D., & Gustafsson, O. (2010).
1146 Extensive methane venting to the atmosphere from sediments of the East Siberian Arctic
1147 Shelf. *Science*, 327, 1246-1249. doi:10.1126/science.1182221

1148 Shakhova, N., Semiletov Igor P., Leifer, I., Sergienko, V., Salyuk, A., Kosmach, D., . . .
1149 Gustafsson, O. (2013). Ebullition and storm-induced methane release from the East
1150 Siberian Arctic Shelf. *Nature Geoscience*, 7, 64-70. doi:10.1038/ngeo2007

1151 Shindell, D. T., Faluvegi, G., Bell, N., & Schmidt, G. A. (2005). An emissions-based view of
1152 climate forcing by methane and tropospheric ozone. *Geophysical Research Letters*, 32,
1153 L04803. doi:doi:10.1029/2004GL021900

1154 Simpson, I. J., Sulbaek Andersen, M. P., Meinardi, S., Bruhwiler, L., Blake, N. J., Helmig, D., . .
1155 . Blake, D. R. (2012). Long-term decline of global atmospheric ethane concentrations and
1156 implications for methane. *Nature*, 488(7412), 490-494. doi:10.1038/nature11342

1157 Solomon, E., Kastner, M., MacDonald, I. R., & Leifer, I. (2009). Considerable methane fluxes to
1158 the atmosphere from hydrocarbon seeps in the Gulf of Mexico. *Nature Geoscience*, 2,
1159 561-565. doi:10.1038/NCEO574

1160 Thompson, D., Leifer, I., Bovensman, H., Eastwood, M., Fladeland, M., Frankenberg, C., . . .
1161 Thorpe, A. K. (2015). Real-time remote detection and measurement for airborne imaging
1162 spectroscopy: A case study with methane. *Atmospheric Measurement Techniques*, 8, 1-
1163 46. doi:10.5194/amtd-8-1-2015

1164 Thornton, B. F., Prytherch, J., Andersson, K., Brooks, I. M., Salisbury, D., Tjernström, M., &
1165 Crill, P. M. (2020). Shipborne eddy covariance observations of methane fluxes constrain
1166 Arctic sea emissions. *Science Advances*, 6(5), eaay7934. doi:10.1126/sciadv.aay7934

1167 Veloso-Alarcón, M. E., Jansson, P., De Batist, M., Minshull, T. A., Westbrook, G. K., Pälike, H.,
1168 . . . Greinert, J. (2019). Variability of acoustically evidenced methane bubble emissions
1169 offshore Western Svalbard. *Geophysical Research Letters*, 46(15), 9072-9081.
1170 doi:10.1029/2019gl082750

1171 Wanninkhof, R., Asher, W. E., Ho, D. T., Sweeney, C., & McGillis, W. R. (2009). Advances in
1172 quantifying air-sea gas exchange and environmental forcing. *Annual Review of Marine*
1173 *Science*, 1(1), 213-244. doi:10.1146/annurev.marine.010908.163742

1174 Washburn, L., Johnson, C., Gotschalk, C. G., & Eglund, E. T. (2001). A gas capture buoy for
1175 measuring bubbling gas flux in oceans and lakes. *Journal of Atmospheric and Oceanic*
1176 *Technology*, 18, 1411-1420. doi:10.1175/1520-0426

- 1177 Weber, D., Marquez, B. A., Taylor, C., Raya, P., Contreras, P., Howard, D., . . . Doezema, L. A.
1178 (2017). Macroseepage of methane and light alkanes at the La Brea tar pits in Los
1179 Angeles. *Journal of Atmospheric Chemistry*, 74(3), 339-356. doi:10.1007/s10874-016-
1180 9346-4
- 1181 Weber, T. C., Mayer, L., Jerram, K., Beaudoin, J., Rzhhanov, Y., & Lovalvo, D. (2014). Acoustic
1182 estimates of methane gas flux from the seabed in a 6000 km² region in the Northern Gulf
1183 of Mexico. *Geochemistry, Geophysics, Geosystems*, 15(5), 1911-1925.
1184 doi:10.1002/2014gc005271
- 1185 Wiggins, S. M., Leifer, I., Linke, P., & Hildebrand, J. A. (2015). Long-term acoustic monitoring
1186 at North Sea well site 22/4b. *Journal of Marine and Petroleum Geology*, 68, 776-788.
1187 doi:10.1016/j.marpetgeo.2015.02.011
- 1188 Wilson, D., Leifer, I., & Maillard, E. (2015). Megaplume bubble process visualization by 3D
1189 multibeam sonar mapping. *Journal of Marine and Petroleum Geology*, 68B, 753-765.
1190 doi:10.1016/j.marpetgeo.2015.07.007
- 1191 Zhao, D., Toba, Y., Suzuki, Y., & Komori, S. (2003). Effect of wind waves on air-sea gas
1192 exchange: Proposal of an overall CO₂ transfer velocity formula as a function of breaking-
1193 wave parameter. *Tellus B: Chemical and Physical Meteorology*, 55(2), 478-487.
1194 doi:10.3402/tellusb.v55i2.16747
1195

1196 **Table of Nomenclature**

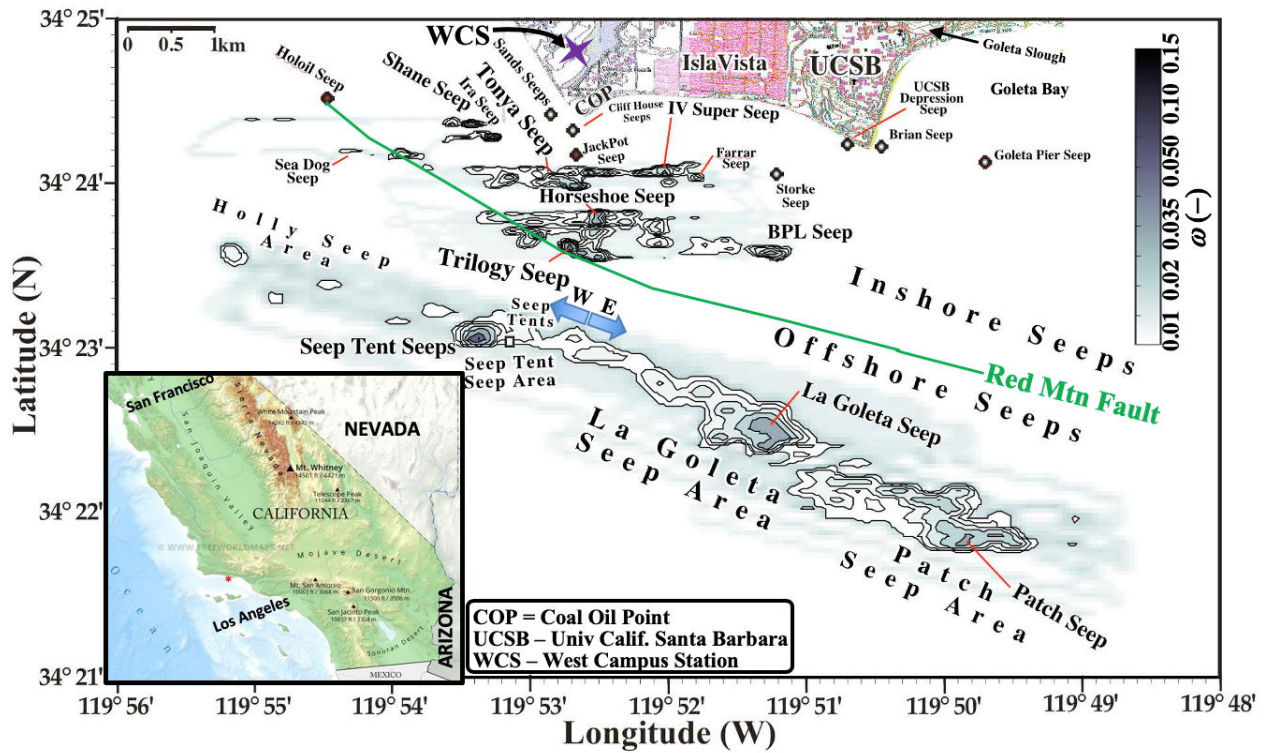
1197	NMHC	Non Methane Hydro Carbons
1198	O&G	Oil and gas
1199	THC	Total hydrocarbon
1200	WCS	West Campus Station
1201	$C_{ave}(\theta)$	Wind direction-resolved average concentration
1202	C_{CH_4}	Methane concentration
1203	$C_{max}(\theta)$	Wind direction-resolved maximum concentration
1204	$C_{med}(\theta)$	Wind direction-resolved median concentration
1205	C'_{Obs}	WCS observed concentration
1206	C_{seep}	Concentration in seep directions
1207	C'_{Sim}	WCS simulated concentration
1208	$u_{ave}(\theta)$	Wind direction-resolved average u
1209	$u_{max}(\theta)$	Wind direction-resolved maximum u
1210	$u_{med}(\theta)$	Wind direction-resolved median u
1211	u_{seep}	Wind speed in seep directions
1212	BL	Boundary layer height
1213	C	Concentration
1214	$C(t, \theta)$	Wind direction and time-resolved average concentration
1215	C'	Plume (anomaly) concentration
1216	C_1 - C_6	Methane to hexane concentrations
1217	E_A	Atmospheric emissions
1218	E_B	Seabed (bottom) emissions
1219	$E_{i,j}$	Grid cell i, j atmospheric emissions
1220	E_W	Emissions to the water column in the near field
1221	i	Grid cell easting index
1222	j	Grid cell northing index
1223	$K(r, \theta)$	Wind direction and distance-resolved correction function to emissions
1224	$K(\theta)$	Wind direction varying, distance correction function to emissions
1225	r	Distance from WCS to cell i, j
1226	R	Residual in C' after Gaussian functional fit
1227	R^2	Correlation coefficient
1228	t	Time
1229	u	Wind speed
1230	$u(\theta)$	Wind direction-resolved wind speed
1231	x, y	Cartesian coordinate system in wind reference frame
1232	Y	Northing offset of WCS
1233	$\delta\theta$	Model wind direction angular resolution
1234	$\phi(u)$	Wind probability distribution
1235	$\phi(\theta, C)$	Wind direction and concentration-resolved probability distribution
1236	$\phi(\theta, u)$	Wind direction and wind speed-resolved probability distribution
1237	$\phi(\omega)$	Sonar return probability distribution
1238	$\phi_i(E_A)$	Normalized atmospheric emissions probability
1239	$\phi_i(\omega)$	Normalized sonar return probability distribution
1240	θ	Wind direction
1241	ω	Sonar return
1242	ψ	Wind veering
1243	ζ	Relative inshore and offshore emissions
1244		

1245

1246 **Table 1. Atmospheric plume composition and model atmospheric emissions.**

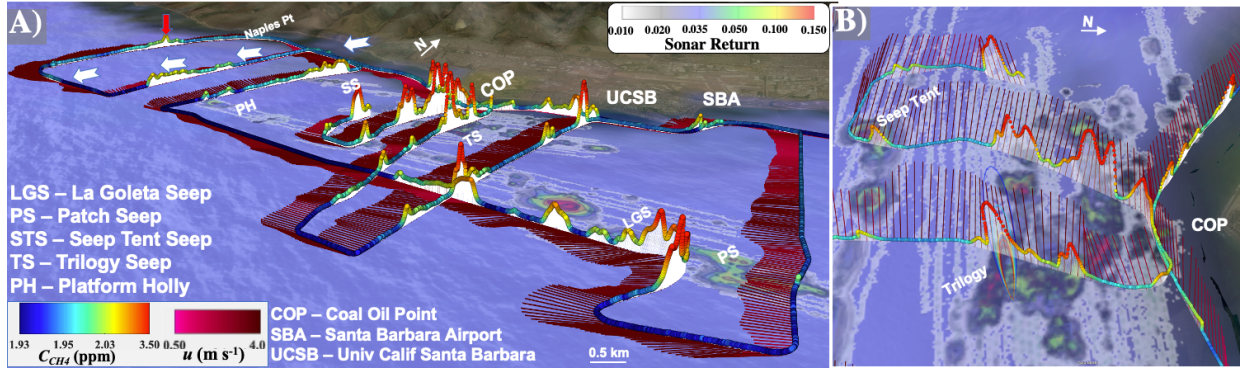
1247	Gas	Fraction	Emissions	Emissions
1248		(%)	(m ³ dy ⁻¹)	(Mg yr ⁻¹)
1249	CH ₄	88.5	73,900	19,300
1250	C ₂ H ₆	3.1	2,590	1270
1251	C ₃ H ₈	4.2	3,510	2520
1252	C ₄ H ₁₀	2.76	2,300	2180
1253	C ₅ H ₁₂	1.11	930	1090
1254	C ₆ H ₁₄	0.13	110	150
1255	C ₆ H ₆	4.4x10 ⁻⁵	4.0	4.7
1256	C ₇ H ₁₆	0.04	33	55
1257	C ₇ H ₈	1.0x10 ⁻⁵	1.0	1.3
1258	NMHC	11.3	9470	7280
1259				
1260	C ₁ -C ₇ *	85	83,400	26,600
1261	CO ₂	15	18,000	12,900
1262	* C ₁ -C ₇ = THC			

1263



1265
 1266
 1267
 1268
 1269

Figure 1: Sonar return, ω , map after Leifer et al. (2010). Purple star marks West Campus Station (WCS). Seep names are informal (Table S3), font size corresponds to strength. E-W arrow segregates east and west offshore seepage. Data keys on panels. Inset shows S. California, red dot marks COP seep field. California inset map from Freeworldmaps (2020).



1270

1271

1272 **Figure 2:** A) COP seep field methane, C_{CH_4} , and wind, u , data for 28 May 2016. White arrows show canyon offshore flow. Red

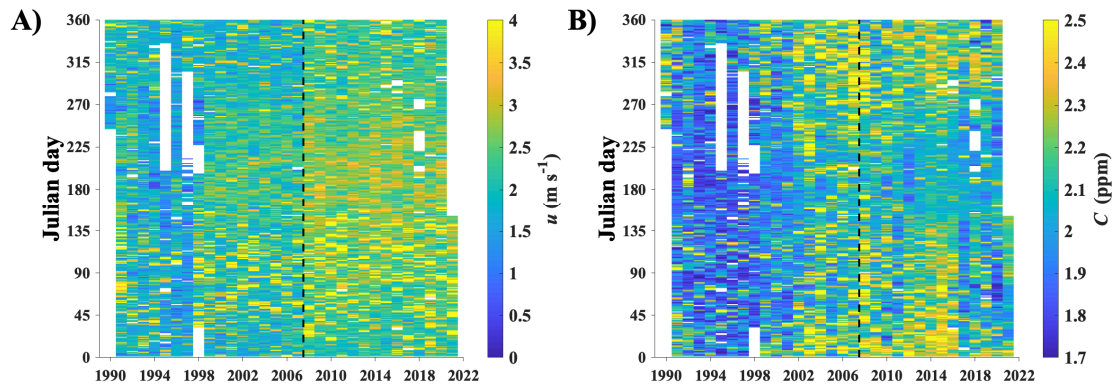
1273 arrows show unmapped seepage to the west of the COP seep field. B) C_{CH_4} and u showing Gaussian plume model for Trilogy Seep.

1274 Sonar return, ω , map in background. Data key and seep name key on panel. Displayed in GoogleEarth environment. See **Supp.**

1275 **Fig. S6** for overhead view.

1276

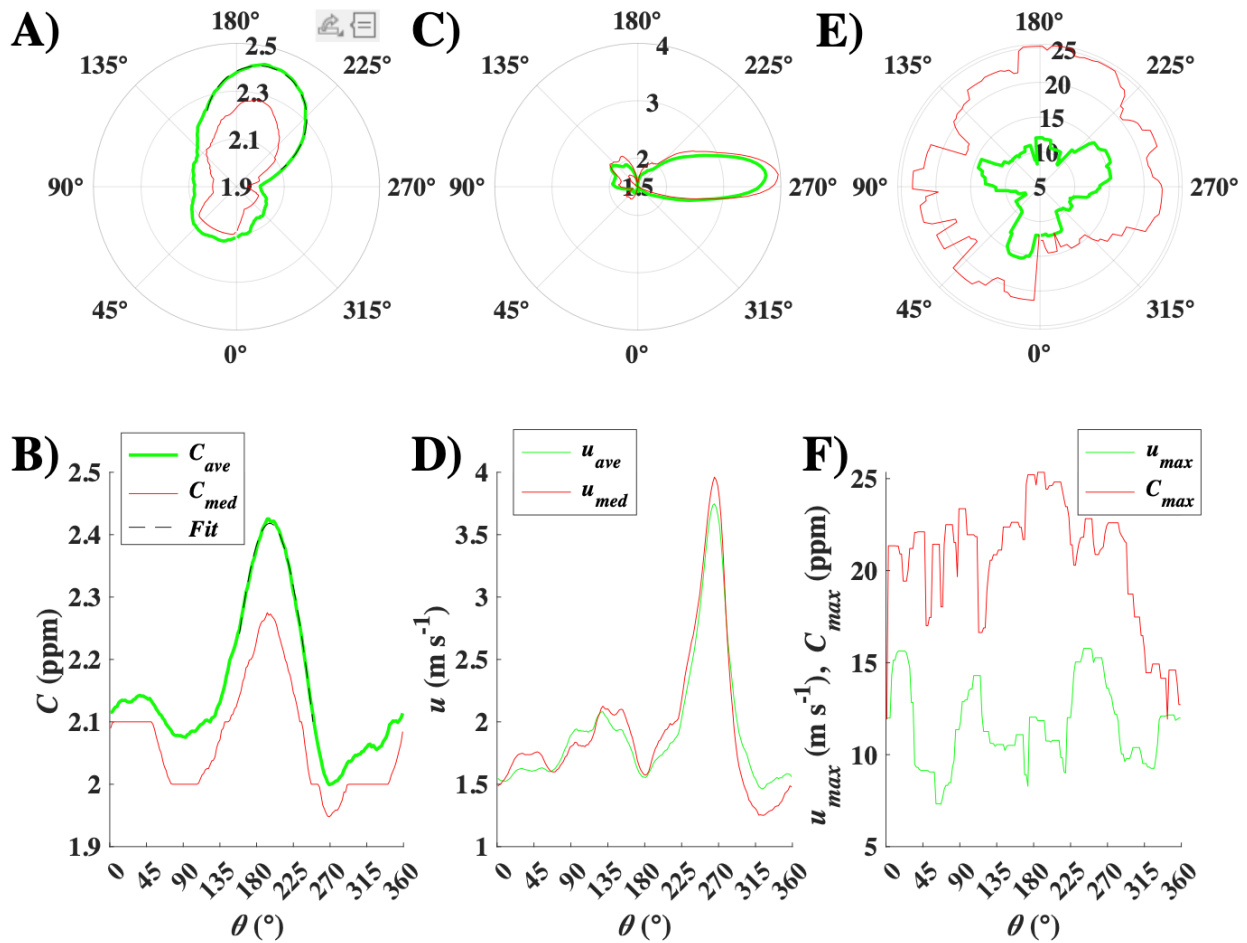
1277



1278
1279
1280

Figure 3: A) Daily mean wind speed, u , and B) concentration, C . Data key on figure. WCS upgrade on Jan 2008 is shown by a dashed black line. **Supp. Fig. S4** shows raw dataset.

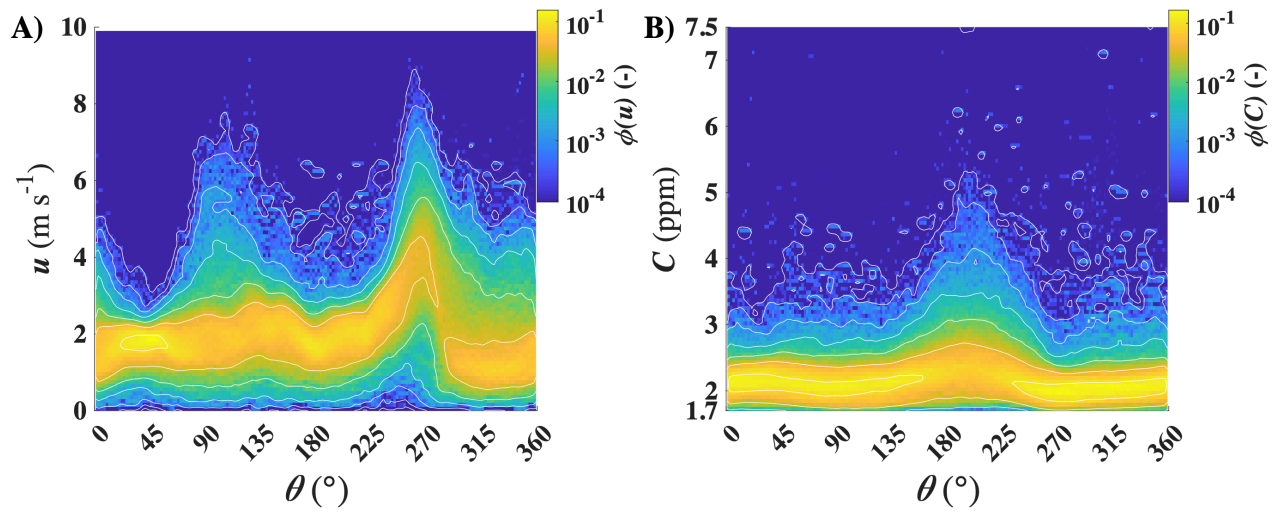
1281



1283
 1284
 1285
 1286
 1287

Figure 4: A, B) Concentration, C , versus wind-direction, θ , 1990-2021 for average, $C_{ave}(\theta)$, and median, $C_{med}(\theta)$, and fit to $C_{ave}(\theta)$ for $155 < \theta < 250^\circ$. Data key on panel B. C, D) Wind speed, u , average, $u_{ave}(\theta)$, and median, $u_{med}(\theta)$, Data key on panel D. and E, F) Maximum C , $C_{max}(\theta)$, and wind speed, $u_{max}(\theta)$. Data key on panel F. Polar plot oriented as at WCS facing the COP seep field.

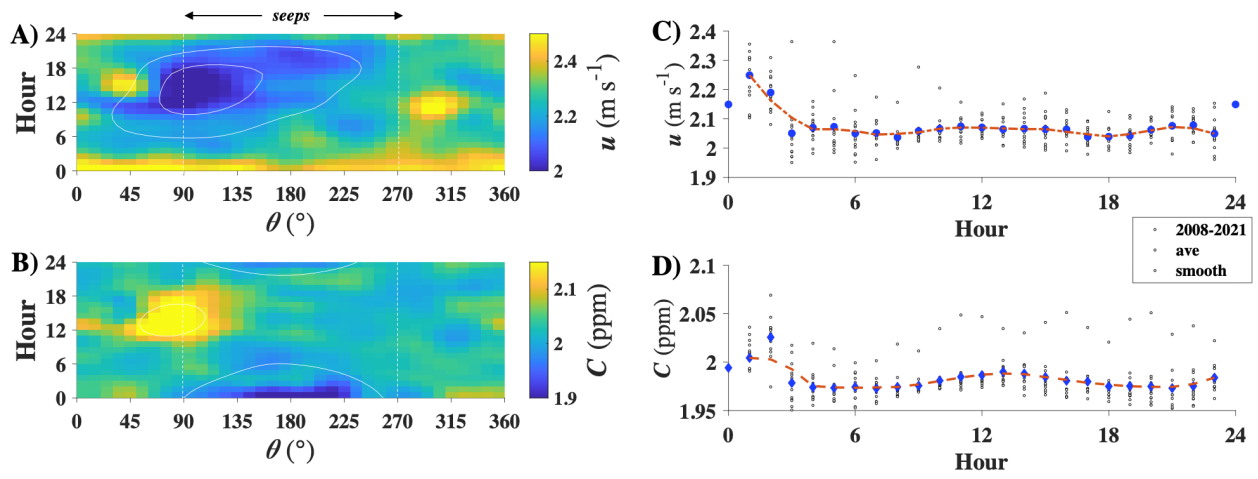
1288



1289
 1290
 1291
 1292

Figure 5: A) Wind-direction (θ) and wind-speed, u , resolved probability distribution, $\phi(\theta, u)$ and B) Concentration probability distribution, $\phi(\theta, C)$, for 1990-2016. White dashed line shows edges of seep field. Data key on figure.

1293



1294

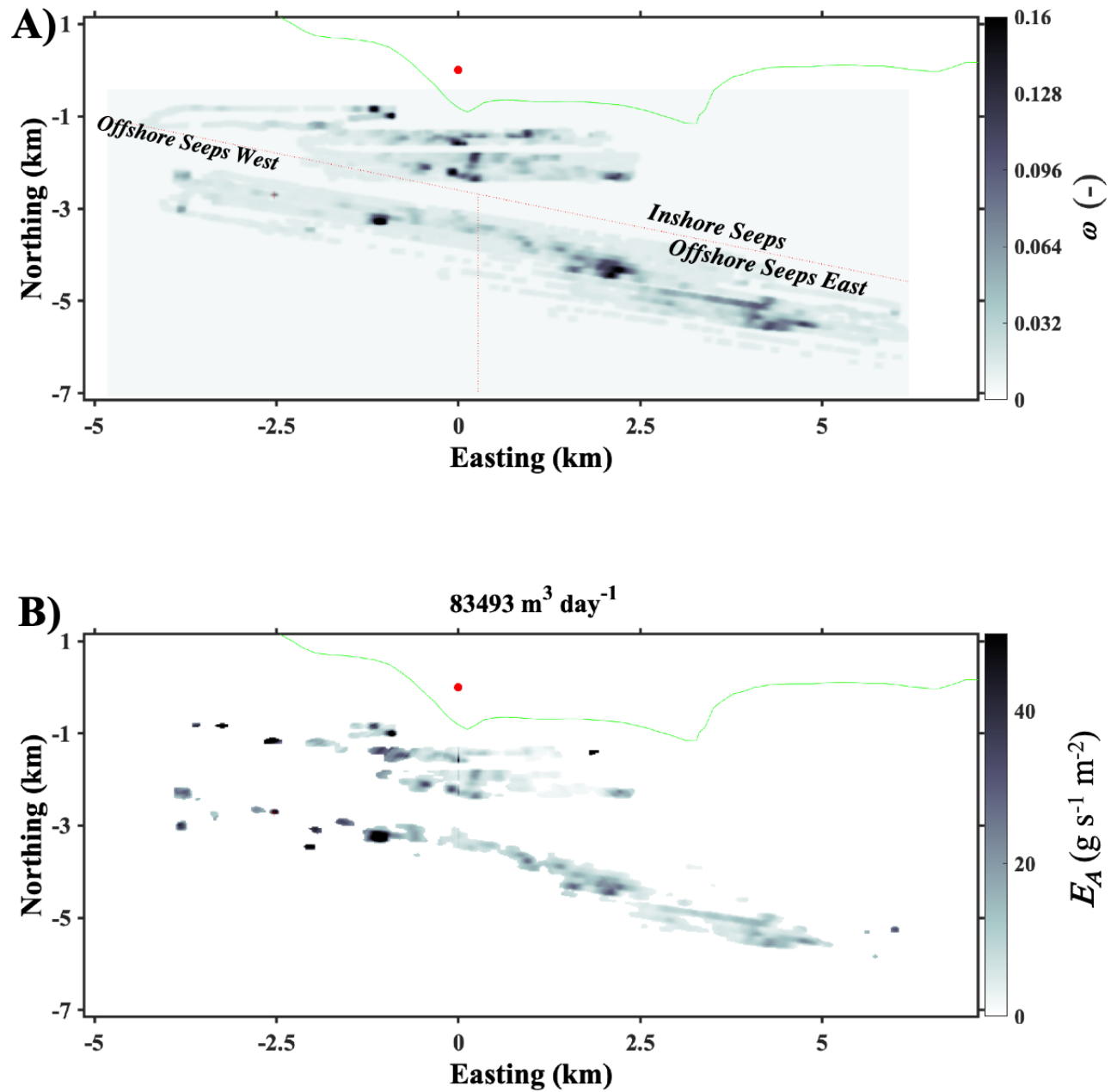
1295

1296

1297

Figure 6: A) 2008-2021 hour- and wind direction-, θ , resolved wind speed, u , and B) concentration, C . C) Hourly-resolved, seep-direction (90–270°), wind speed, u , and D) concentration, C , averaged, individual years, and 3-year smoothed. Data key on figure. Midnight data missing due to daily calibration.

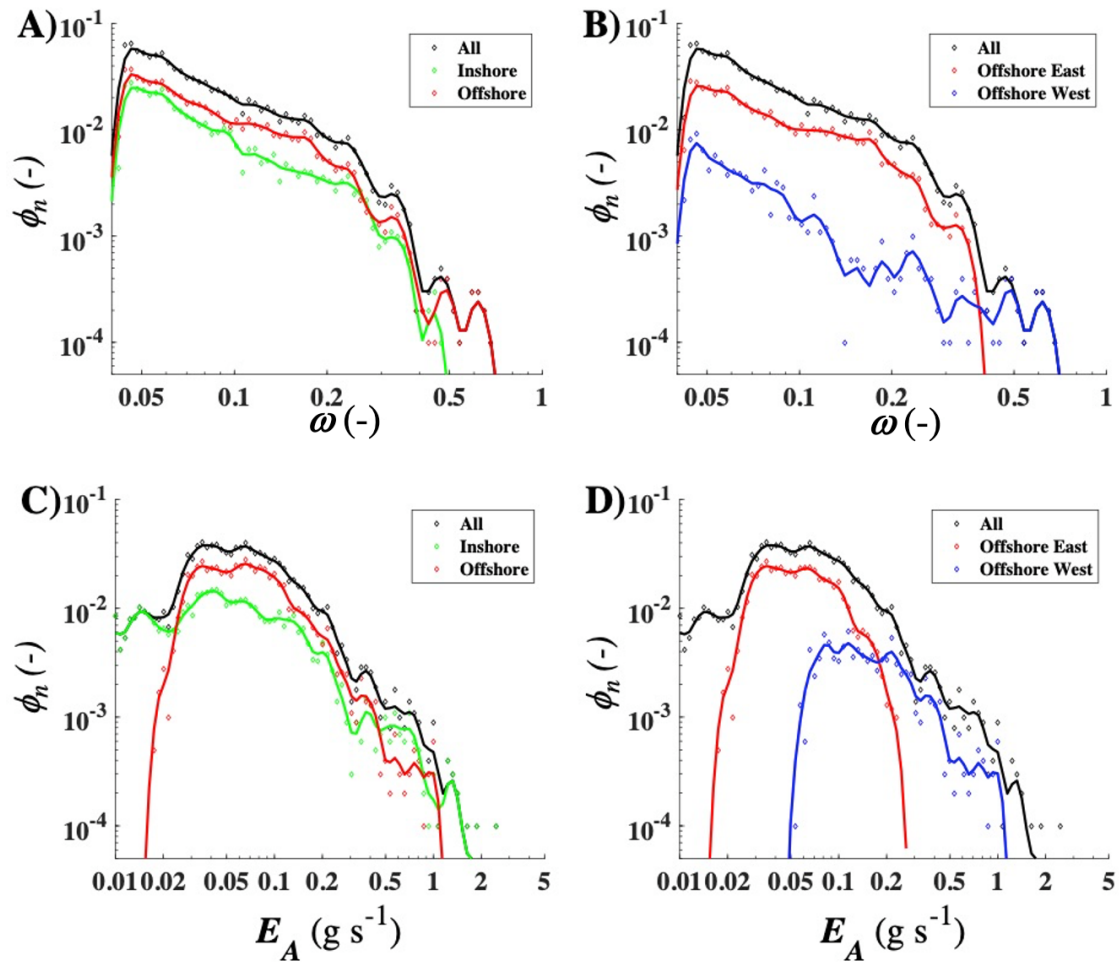
1298



1299
 1300
 1301

Figure 7: **A)** Sonar return, ω , gridded at 22-m resolution. **B)** Atmospheric emissions, E_A . West campus station (red dot) is at coordinate system origin. Green line is coast line.

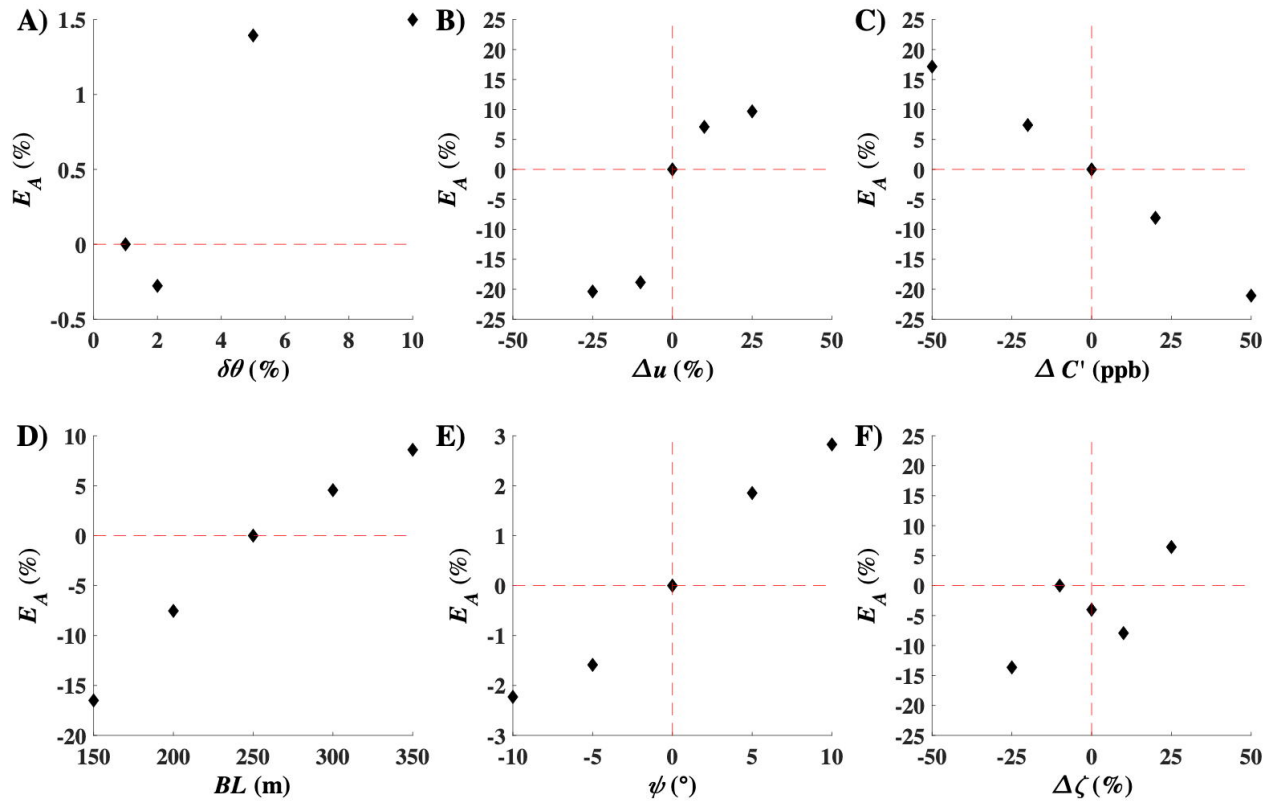
1302



1303
 1304
 1305
 1306
 1307

Figure 8: A) Sonar return, ω , occurrence probability, $\phi_n(\omega)$, for all seepage, inshore and offshore seepage and B) all seepage, offshore east seepage, and offshore west seepage. C) Atmospheric emission, E_A , occurrence probability, $\phi_n(E_A)$, for all seepage, inshore and offshore seepage and D) all seepage, offshore east seepage, and offshore west seepage. Data key on panels.

1308



1309

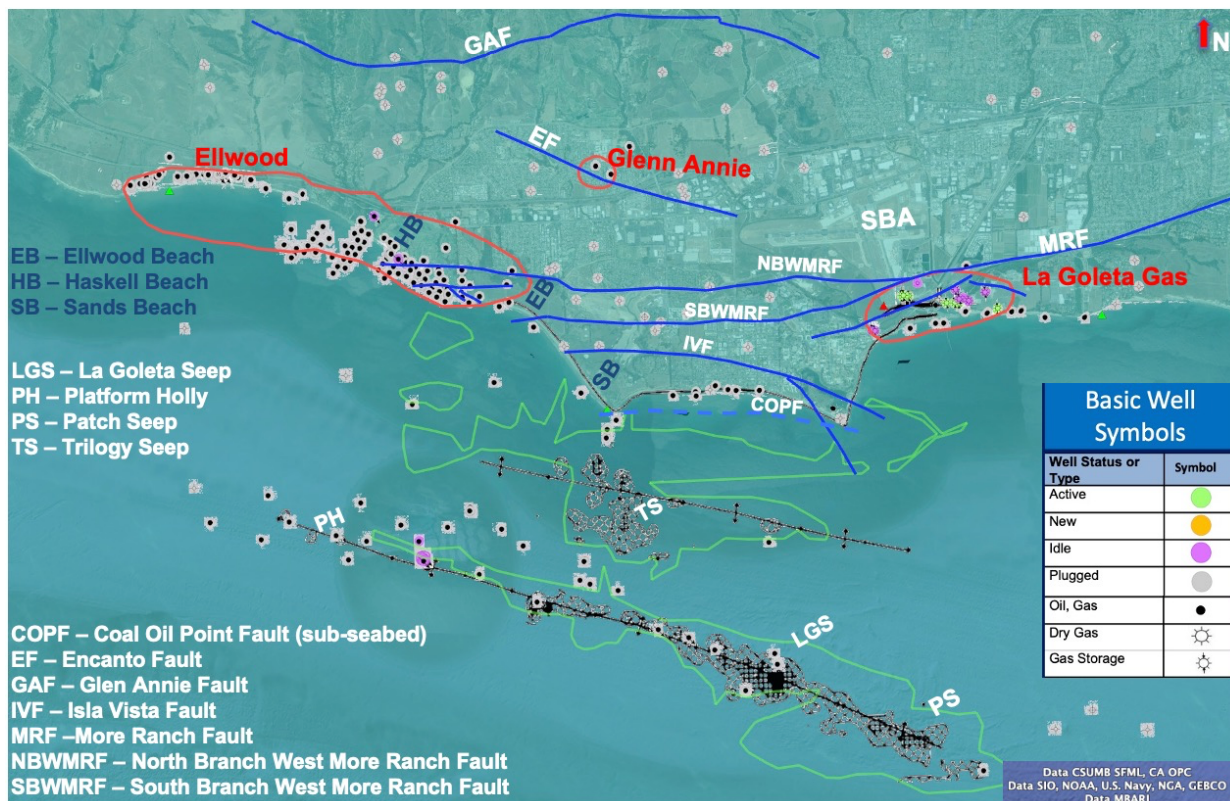
1310

1311

1312

Figure 9: Emissions, E_A , sensitivity to uncertainty in A) model angular resolution, $\delta\theta$, B) wind speed variation, Δu , C) concentration anomaly variation, $\Delta C'$, D) boundary layer thickness, BL , E) wind veering, ψ , and F) inshore/offshore partition variation, $\Delta\zeta$. Note different units on different plots. See text for details.

1313



1314
 1315
 1316
 1317

Figure 10: Map of the Goleta Plains oil and gas fields, wells, and the Coal Oil Point (COP) seep field. Grey hatch shows 1995 field extent, green outlines the 1940 field extent is from Leifer (2019). Field locations from Olson (1983). Well data from CDOGGR (2018). Faults from Minor et al. (2009). Seep names are informal. Data keys on panels. Shown in the Google Earth environment.